University of Central Florida

STARS

2020

Few-Mode Fiber Lasers and Amplifiers

Ning Wang
University of Central Florida

FEW-MODE FIBER LASERS AND AMPLIFIERS

by

NING WANG

B.S. Beijing University of Posts and Telecommunications, 2011

M.S. Beijing University of Posts and Telecommunications, 2014

A dissertation submitted in partial fulfillment of the requirements

for the degree of Doctor of Philosophy

in CREOL / The College of Optics and Photonics

at the University of Central Florida

Orlando, Florida

Fall Term

2020

Major Professor: Guifang Li

ABSTRACT

Lasers and amplifiers of high-order spatial modes are useful for a number of applications, including communication, sensing, microscopy, and laser material processing. This dissertation presents the generation and amplification of high-order spatial modes in few-mode fibers (FMFs).

In the area of amplification of high-order spatial modes, low-crosstalk amplification among spatial modes is realized in a retro-reflecting few-mode Er-doped fiber amplifier (EDFA) by exploiting the unitary property of the coupling matrix of a symmetric photonic lantern (PL). A small-signal gain larger than 25 dB and crosstalk below -10 dB was achieved over the C-band for a 3-mode EDFA. Such a few-mode EDFA can replace multiple parallel single-mode EDFAs in single-mode fiber transmission systems. In addition, we presented an EDFA for orbital angular momentum (OAM) modes using an annular-core PL. Both the first- and second-order OAM modes were amplified with nearly 20 dB of gain over the C-band.

Placing a few-mode EDFA and a mode-selective PL inside a linear cavity, we demonstrated an intra-cavity transverse mode-switchable fiber laser for the generation of high-order spatial modes. The six linearly-polarized (LP) modes can lase independently and are switchable by changing the input port of the PL. In addition, we generated donut-shaped beams using incoherent superposition and simultaneous lasing of the two degenerate modes in the same LP mode group.

Additional techniques for the generation of high-order modes explored in this thesis utilize stimulated Brillouin scattering (SBS), one of the prominent nonlinear effects in optical fibers. Based on backward SBS in a passive FMF, we experimentally demonstrated a transverse mode-

selective Brillouin fiber laser using mode-selective PLs. We generated three LP modes via both intra- and inter-modal SBS.

Finally, we propose a fiber ring cavity that can simultaneously produce phonon lasing and photon lasing utilizing forward intermodal SBS. We experimentally demonstrated for the first time, to the best of our knowledge, such a two-domain ring laser using a 10-meter reduced-cladding two-optical mode fiber. By using an LP_{01} optical pump, both the LP_{11} Stokes lightwave and a low-frequency flexural acoustic wave can be amplified by stimulated emission and oscillate inside the same fiber ring cavity. The measured photon laser beat linewidth and the phonon laser linewidth are on the order of a few kHz.

To My Parents

ACKNOWLEDGMENTS

First and foremost, I would like to express my sincere gratitude to my adviser, Dr. Guifang Li for being a great mentor during my PhD study at CREOL. Dr. Li has been extremely patient and helpful during my PhD study and research. What I learned from him is not only the knowledge, but also how to focus on the research projects, and make progress step by step until the completion. There is no doubt that without him, there is no way for me to finish my PhD alone.

I would also like to thank my co-advisor, Dr. Rodrigo Amezcua-Correa. I could still remember the first time when I entered him lab, I didn't know how to operate any of those equipment. Dr. Rodrigo taught me almost everything from the beginning to the end of the experiment. His instructions were really helpful for me in my subsequent years when I was doing experiments independently.

I would also like to thank my collaborators outside CREOL, including Inwoong Kim, Olga Vassilieva, Tadashi Ikeuchi from Fujitsu lab; Pierre Sillard, Adrian Amezcua-Correa, Cedric Gonnet from Prysmian Group; and Sergio Leon-Saval from the University of Sydney. They provided tremendous supports and helpful discussions to my research work.

I am deeply grateful to my dissertation committee members, Dr. Axel Schülzgen and Dr. Debashis Chanda, for their helpful guidance and time.

I would like to thank the postdocs and research scientists in my group, He Wen, S. Chandrasekhar, Jose Enrique Antonio-Lopez, Daniel Cruz Delgado, Md Selim Habib, for their assistance in both theoretical analysis and experimental demonstrations.

I would also like to thank every graduate student in my group, including Bin Huang, Huiyuan Liu, Shengli Fan, Rachel Sampson, Yuanhang Zhang, Alireza Fardoost, Juan Carlos Alvarado-Zacarias, Steffen Wittek, Stefan Gausmann. We always help and support each other, and the working environment are always friendly.

Lastly but most importantly, I would like to express my deepest gratitude to my family for their constant encouragement and support throughout my studying abroad.

TABLE OF CONTENTS

LIST OF FIGURES

xiii

LIST OF TABLES

CHAPTER 1   INTRODUCTION

1.1 High-Order Spatial Mode Lasers and Amplifiers

Optical fibers with large mode areas can support high-order linearly-polarized (LP) modes with various spatial intensity distributions. High-order transverse mode lasers, together with their amplifiers, are beneficial for a number of applications. For example, high-order LP modes in optical fibers with larger effective areas have higher thresholds for detrimental nonlinear impairments compared to the fundamental mode [1]. It has also been shown that high-order modes can reduce sensitivity to mode profile distortion [2], as well as improve energy extraction in high-power pulsed laser systems. There are other important applications that require high-order modes (HOMs). In mode-division multiplexed fiber communication systems, when each LP mode in the few-mode fiber (FMF) is used to transmit an individual data stream, the total transmission capacity can be significantly increased [3-6]. In fiber sensor systems, high-order LP modes in the FMF allow the measurement sensitivities of multiple sensing parameters, including bending curvature, temperature and strain, to be increased [7-10]. In material processing, lasers with specific beam profiles can be used to process surfaces as desired [11], as well as improve the processing speed [12] and get a higher cutting quality [13]. In addition, recent research has indicated that HOM lasers are advantageous for the detection of gravitational waves because they can reduce the thermal noise significantly [14, 15].

1.2 Existing Approaches

Due to their unique properties and advantages in many different kinds of applications, methods for generating and amplifying specific HOMs have attracted increased interest within the laser community in the past decade.

Several techniques have been implemented successfully to generate lasing at specific HOMs. Using few-mode fiber Bragg grating (FBG) and a tunable filter, it is possible to select one of the two lowest LP modes [16-18]. Lasing at the two lowest LP modes can also be achieved by employing a polarization discriminating element [19]. Another approach involves achieving dynamic intra-cavity beam control with an electronically-addressable deformable mirror [20]. However, using each method above, it was not possible to produce lasing with modes beyond the first two LP fiber modes due to the limited resolution of the intra-cavity mode selective elements. In addition, a "digital laser" employing a software-defined spatial light modulator (SLM) has been demonstrated to generate desired laser mode patterns [21, 22], but the laser efficiency is fairly low owing to the high loss of the SLM. Another laser with high-order Hermite-Gaussian (HG) modes has been demonstrated, namely, a Yb: phosphate laser based on an off-axis pumping technique [23].

Lasers with donut-shaped intensity profiles can be considered as the superposition of two degenerate modes. Donut-shaped lasers carrying orbital angular momentum (OAM) associated with spiral phase profiles can be generated by tailoring the pump intensity distribution [24-26] or by placing a set of phase plates inside a folded cavity [27]. Recently, an intra-cavity donut mode laser was reported that was generated based on an incoherent superposition of two degenerate petal modes lasing together in the same cavity [28]. Donut-shaped profile lasers can also be generated

in an all-fiber laser structure by using intra-cavity mode-selective elements, such as mode-selective couplers [29, 30] or long-period two-mode FBG [31].

The fiber amplifiers for HOMs have also been investigated intensively in the past decade, especially the inline few-mode erbium-doped fiber amplifier (EDFA) [4] and Raman amplifier [32], which are essential for long-haul spatial-division multiplexed fiber communication systems. It is necessary to make sure that the gains of all spatial modes are nearly equal for a FMF amplifier. In the few-mode EDFA, this near-equality can be realized by controlling the pump mode profiles, tailoring the doping concentration profile, or using a cladding pumping scheme [33-37]. An EDFA capable of amplifying 21 spatial modes with over 15 dB of gain for the entire C-band and a differential modal gain of less than 3 dB has been demonstrated [38]. Apart from their application in communication systems, the fiber amplifiers for HOM lasers could also be used as power combiners in high-power laser systems [39].

1.3 Dissertation Outline

The outline of this dissertation is given below:

In chapter 2, we propose a low-crosstalk few-mode EDFA by exploiting the unitary property of the coupling matrix of a symmetric photonic lantern (PL). This few-mode EDFA can replace multiple parallel single-mode EDFAs. We demonstrate a 3-channel few-mode EDFA using the retro-reflection of a 3-mode symmetric PL experimentally.

In chapter 3, we present an EDFA for OAM modes using an annular-core PL. Both the first- and second-order OAM modes are amplified with a small-signal gain of around 20 dB. The mode profiles are maintained after amplification, and this scheme works for the entire C-band.

In chapter 4, we demonstrate an intra-cavity transverse mode-switchable fiber laser based on a mode-selective PL and a few-mode Er-doped fiber amplifier experimentally. The six lowest-order LP modes can lase independently and can be switched by changing the input port of the PL. In addition, we demonstrate donut-shaped LP_{11} and LP_{21} modes using the incoherent superposition and simultaneous lasing of the two degenerate modes.

In chapter 5, we demonstrate a transverse mode-selective few-mode Brillouin fiber laser utilizing mode-selective PLs experimentally. We generate the lowest three orders of the LP modes based on both intra- and inter-modal SBS effects in the passive FMF.

In the last chapter, we propose a fiber ring cavity that can simultaneously produce phonon lasing and photon lasing utilizing forward intermodal SBS. We also demonstrate such a two-domain ring laser using a 10-meter reduced-cladding two-optical-mode fiber experimentally. Using an LP_{01} optical pump, both the LP_{11} Stokes lightwave and a low-frequency flexural acoustic wave can be amplified via stimulated emission and oscillate inside the same fiber ring cavity.

CHAPTER 2   LOW-CROSSTALK FEW-MODE EDFA FOR SINGLE-MODE FIBER NETWORKS

2.1 Introduction

Space-division multiplexing (SDM) technology has attracted serious attention in the past decade as a promising scheme to overcome the capacity crunch in single-mode fiber (SMF) communication systems [3, 40]. To date, several transmission experiments including using mode-division multiplexing (MDM) in FMFs, or core multiplexing in multicore fibers (MCFs) have been reported [41-44]. EDFAs for SDM systems are highly desirable since they are essential for long-haul transmissions. Alternatively, one SDM based EDFA can replace several parallel single-mode EDFAs, thus reducing the overall cost of SMF trunk transmission lines or networks.

Multicore EDFA is one typical type of the SDM amplifiers that can be realized by using fan-in/fan-out devices as the signal combiner. With cladding pump configuration, it offers lower cost solution through components integration and the use of single high-power pump diode [45-48]. However, the pump conversion efficiencies were usually very low for this type of EDFAs. Few-mode EDFA (FM-EDFA) is another option. It could be made by free space optics, to convert the signal into high-order modes by using phase plates, and combine them through beam splitters [4, 33, 37]. But the combining loss would be pretty large in this case. In the recent few years, all-fiber photonic lantern (PL) based FM-EDFA has attracted more interests due to its low-loss feature. This type of amplifiers supporting 6-10 spatial channels have been experimentally demonstrated [35, 49]. However, the crosstalk between different channels is seems inevitable even with a mode-selective photonic lantern (MSPL), this is because of the high crosstalk (around -3 dB) between degenerate modes.

In this section, we propose and experimentally demonstrated a low-crosstalk FM-EDFA exploiting the unitary property of the coupling matrix of the PL. We show theoretically that mode crosstalks can be suppressed in a retro-reflection configuration even if a non-mode-selective PLs are used for (de)multiplexing. Experimentally, we demonstrated a low-crosstalk 3-mode EDFA even though a high-crosstalk 3-port symmetric PL was used as the spatial (de)multiplexer. The small signal gain of all three channels are greater than 25 dB and the crosstalk of each channel is lower than -10 dB.

2.2 Principle and Theoretical Analysis
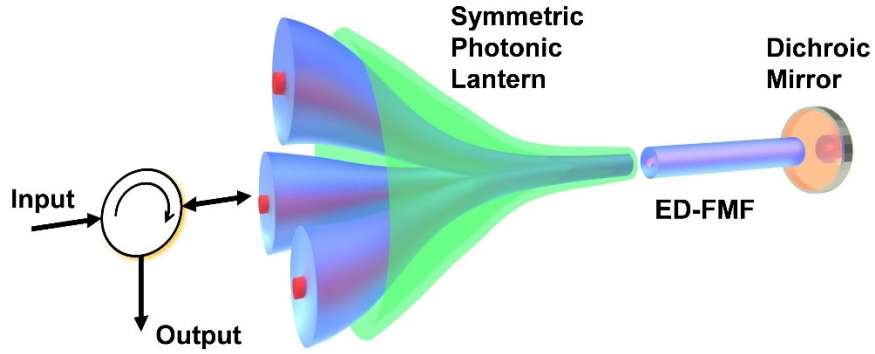
Figure 2-1: Schematic setup of the low-crosstalk FM-EDFA based on the retro-reflection of a symmetric PL.

The schematic setup of the proposed FM-EDFA with low crosstalk is shown in Fig. 2-1. Each input signal is launched into one port of a symmetric PL through a circulator. At the output of the PL, the signal is amplified by the erbium-doped few-mode fiber (ED-FMF). The resulting signal is reflected back by a dichroic mirror (DM) and amplified by the ED-FMF again in the reverse direction before being coupled out through the PL and the circulator. The relationship

6

between the input signal amplitudes $\boldsymbol{A}_{in}$ and output signal amplitudes $\boldsymbol{A}_{out}$ can be expressed as following:

$$\boldsymbol{A}_{out} = \boldsymbol{M}_{MUX}^T \cdot \boldsymbol{G}^T \cdot \boldsymbol{G} \cdot \boldsymbol{M}_{MUX} \cdot \boldsymbol{A}_{in} \tag{2-1}$$

where the matrix $\boldsymbol{M}_{MUX}$ is the mode transfer matrix of the symmetric PL. For a lossless PL, it is real and unitary [50]. For example, the matrix for a 3-to-1 symmetric PL can be written as [51]:

$$\boldsymbol{M}_{MUX} = \begin{bmatrix} 1/\sqrt{3} & 1/\sqrt{3} & 1/\sqrt{3} \\ \sqrt{2/3} & -1/\sqrt{6} & -1/\sqrt{6} \\ 0 & 1/\sqrt{2} & -1/\sqrt{2} \end{bmatrix} \tag{2-2}$$

The matrix $\boldsymbol{G}$ is the mode coupling matrix of the ED-FMF. The coupling length is usually on the order of tens of meters for degenerate modes [5] and on the order of kilometers for nondegenerate modes [52], after which the mode coupling could be observed. For a short length of fiber (a few meters), it can be assumed to be a diagonal matrix. In general, the gain value of each mode of a FM-EDFA are not equal. For the 3-LP mode ED-FMF, it can be expressed as:

$$\boldsymbol{G} = \begin{bmatrix} g_1 e^{i\Delta\varphi} & 0 & 0 \\ 0 & g_2 & 0 \\ 0 & 0 & g_3 \end{bmatrix} \tag{2-3}$$

where $\Delta\varphi$ is the propagation phase difference between the two mode groups:

$$\Delta\varphi = \Delta n_{eff} \frac{2\pi}{\lambda} L \tag{2-4}$$

and Δn_{eff} is the effective index difference between the two mode groups, λ is the signal wavelength and L is the total length of the ED-FMF. One can easily verify that when the gain of all spatial modes are equal to g_0, and the phase difference $\Delta\varphi$ is zero, the total transfer matrix of

7

the system will be a diagonal matrix $g_0^2 \cdot \boldsymbol{I}$ because of the unitary property of $\boldsymbol{M}_{MUX}$. That means there will be no channel crosstalk.
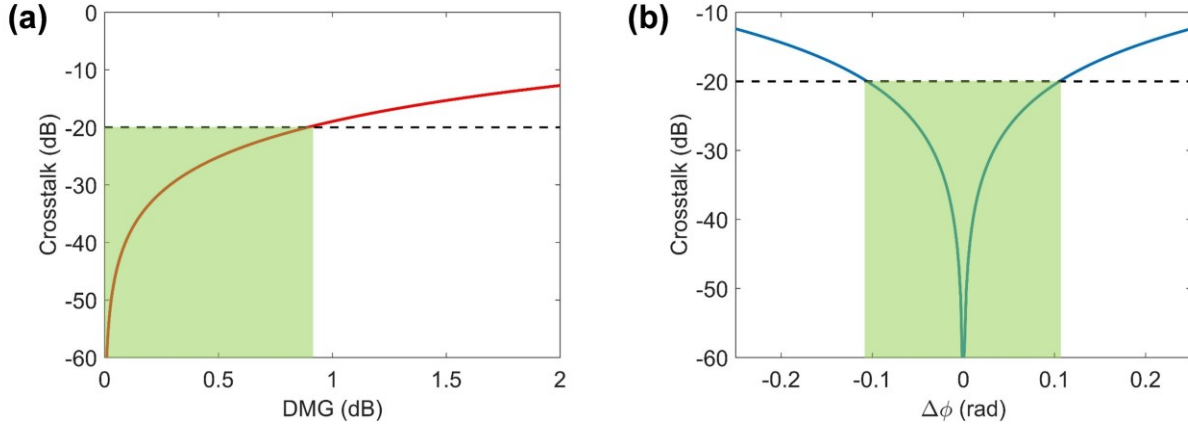
Figure 2-2: (a) Calculated channel crosstalk with the increase of DMG between the first two LP modes, (b) crosstalk vs. phase difference between the first two mode groups in the ED-FMF.

However, because of differential modal gain (DMG) and modal dispersion, both amplitude and phase of the elements in matrix $\boldsymbol{G}$ are not always equal. We simulated the effect of DMG on the crosstalk for a three channel system, and the result is shown in Fig. 2-2(a). We can see that the crosstalk increases as the DMG grows. In order to suppress the crosstalk to below -20 dB, the DMG needs to be less than 1 dB. We also investigated the effect of phase difference between the first two mode groups on the crosstalk, as shown in Fig. 2-2(b). It indicated that in order to suppress the crosstalk to below -20 dB, the phase difference $\Delta\varphi$ should be within $m\pi \pm \pi/25$.

2.3 Proof-of-Concept Experiment

The active fiber used in our proof-of-concept experiment was an ED-FMF fabricated in house. Figure 2-3(a) shows the measured refractive index profile of this fiber, and its cross-sectional microscope image is shown in Fig. 2-3(b). It is a step-index fiber with a core and cladding

8

diameter of 10 μm and 125 μm, respectively. The numerical aperture (NA) of this ED-FMF was measured to be 0.24, ensuring it supports 3 linearly-polarized (LP) modes at the signal wavelength, and supports one more mode group at the pump wavelength. The core area was doped with pure erbium ions at a concentration of ~4.5×10^{25} m^{-3}, that can provide a maximum gain of nearly 10 dB/m for each spatial mode at 1550 nm.
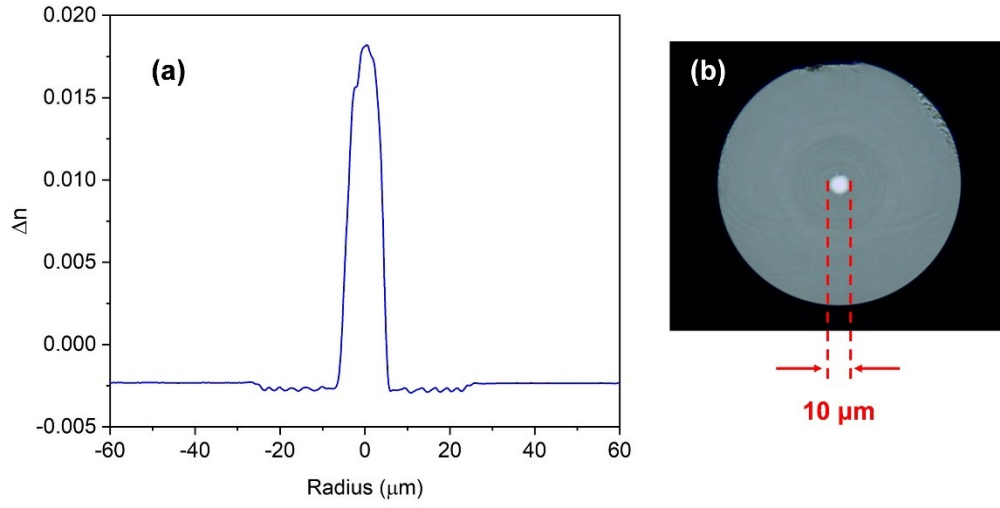
Figure 2-3: (a) Measured refractive index profile, and (b) cross-sectional microscope image of the 3-mode ED-FMF used in our low-crosstalk FM-EDFA experiment.

The modal gain of a FM-EDFA is essentially determined by the degree of overlap between the doping profile, and the pump and signal mode intensity profiles [34, 53], which can be expressed as:

$$\eta_{i,j} = \iint \Gamma_{s,i}(r,\varphi) \, \Gamma_{p,j}(r,\varphi) N_0(r,\varphi) r dr d\varphi \qquad (2-5)$$

where $\Gamma_{s,i}(r,\varphi)$ and $\Gamma_{p,j}(r,\varphi)$ are the normalized intensity distribution of i-th signal mode and j-th pump mode inside the ED-FMF and $N_0(r,\varphi)$ is the doping profile of the gain fiber, which is uniformly doped for our gain fiber. We further calculated the value of the overlap integrals for

different pump and signal mode pairs in our ED-FMF, and the results are shown in Table 2-1. We find that by using LP_{11} mode as the pump, the values for the two signal modes are almost the same, which means the DMG is minimized. It should be noted that by using LP_{11} mode as the pump, because of the intensity distribution is not uniform at the transverse plane, there will be slightly fiber refractive index perturbation. But this perturbation will not create any mode coupling.

Table 2-1. Overlap integrals of the normalized intensity profile of the ED-FMF.

$\eta_{i,j}$	$LP_{01,s}$	$LP_{11,s}$
$LP_{01,p}$	2.01×10^{10}	1.31×10^{10}
$LP_{11,p}$	1.45×10^{10}	1.51×10^{10}
$LP_{21,p}$	1.13×10^{10}	1.48×10^{10}

We use a 3-to-1 symmetric PL as the signal combiner. To fabricate a PL device, multiple SMFs were inserted into a fluorine-doped capillary tube whose refractive index is lower than that of the SMF cladding. The tube was adiabatically tapered down to create a FMF output at the taper waist, and the modes were guided inside the SMF cladding area [54]. The schematic cross-sectional view of the input of a 3-to-1 symmetric PL is shown in Fig. 2-4(a). It contains three identical graded-index SMFs whose core and cladding diameter is 14/125 μm. After tapering, the resulting FMF has a core and cladding diameter of 18/90 μm. We measured the output mode profiles of each port of the symmetric PL at the signal wavelength by a CCD camera, the results are shown in Fig. 2-4(b). All of them are superpositions of the LP_{01} and LP_{11s} modes. The insertion losses of three channels were measured to be -1.2 dB, -0.9 dB and -0.7 dB, respectively. The insertion losses of the PL mainly come from the imperfection of the tapering process. If the loss for each mode are equal, it will not affect the crosstalk performance. However, the mode-

dependent loss is always inevitable. This will cause the mode coupling matrix slightly off from a unitary matrix, and further affect the crosstalk performance.
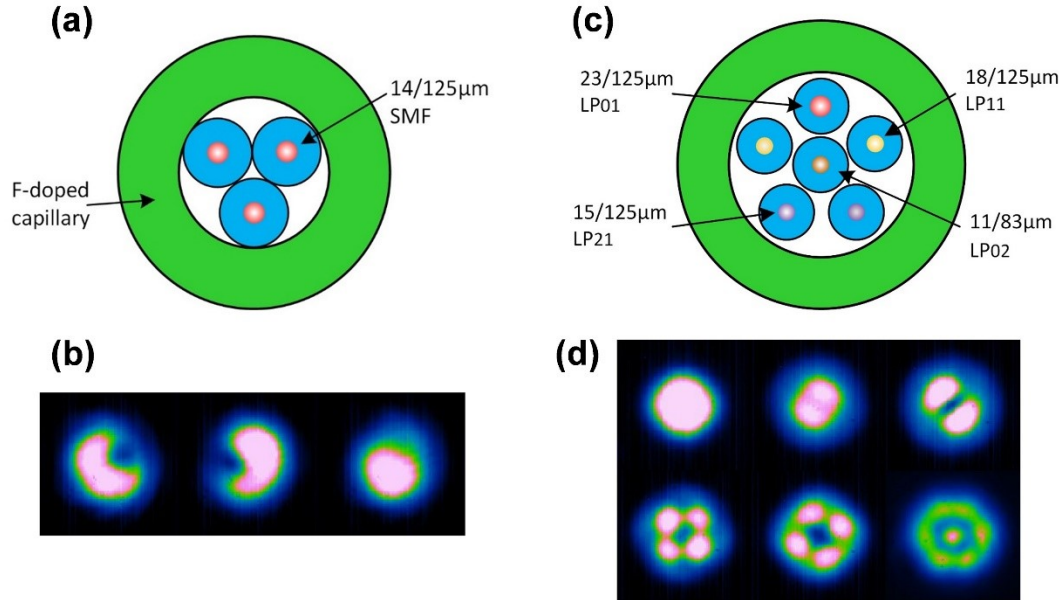
Figure 2-4: (a) cross-sectional view of the input fiber distribution for the 3-to-1 symmetric PL, (b) output mode profiles of the 3-mode symmetric PL measured at 1550 nm, (c) cross-sectional view of the input fiber distribution for the 6-mode MSPL, (d) mode profiles of the 6-mode MSPL measured at 976 nm.

We also fabricated a 6-mode MSPL for the spatial pump mode control. To achieve mode selective feature, we should use dissimilar SMFs at the input. Each input fundamental mode evolves into a particular LP mode at the output FMF based on the propagation constant matching condition [55-57]. The cross-sectional profile of a 6-mode MSPL is shown in Fig. 2-4(c). It contains 6 graded-index fibers with core diameters of 23, 18, 18, 15, 15, and 11μm, that map to the LP_{01}, LP_{11a}, LP_{11b}, LP_{21a}, LP_{21b}, and LP_{02} mode, respectively. At the output side, the resulting FMF's core diameter is 20 μm. We also measured the output mode profiles of the MSPL at the pump wavelength, as shown in Fig. 2-4(d). The mode patterns of the 6 lowest LP modes were clearly observed.
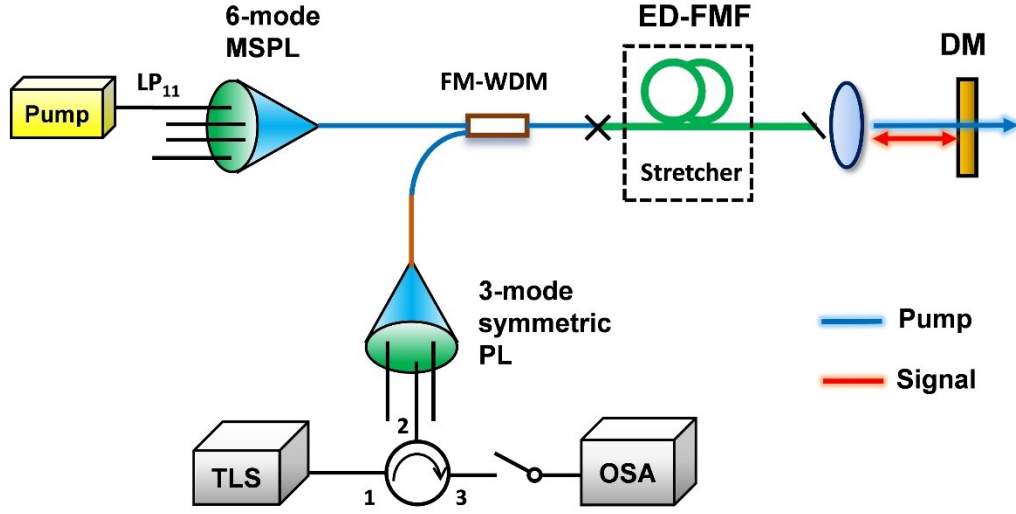
Figure 2-5: Experimental setup of the FM-EDFA with reduced channel crosstalk in a 3-mode symmetric PL. DM: dichroic mirror; TLS: tunable laser source; OSA: optical spectrum analyzer.

The experimental setup of the low-crosstalk FM-EDFA is shown in Fig. 2-5. The signal emitted from the tunable laser source (TLS) was launched into the port 1 of the circulator, and further went into the 3-to-1 symmetric PL from port 2. The input signal power was set to be -20 dBm at the wavelength of 1550 nm. The pump light from a 976 nm pump diode was launched in to a 6-mode MSPL for the pump mode control. Here we used LP_{11} mode as the pump for the gain equalization. The output of the two PLs were spliced with a 980/1550 nm FM-WDM coupler. The FM-WDM was made of 6-LP mode FMFs whose core and cladding diameter is 16/125 μm based on free space optics. It contains three fiber collimators that fixed at the FMF ends and a DM inside a 3-cm long tube. The output of the FM-WDM was further spliced to the ED-FMF. The length of the gain fiber is 2.5 meters, which was angle cleaved. We slightly stretched the ED-FMF to adjust the phase difference in order to suppress the channel crosstalk, as discussed above. The amplified signal at the output of the ED-FMF was reflected by another DM, and coupled back into the ED-FMF and amplified again in the reverse direction. The resulting signal was coupled out from the

three single-mode ports of the symmetric PL. The port under test is detected through port 3 of the circulator. An optical spectrum analyzer (OSA) was used to measure the output optical powers and spectrums of all 3 ports of the PL.

We characterized the net gain of each channel of the amplifier system. The results of all the three channels are shown in Fig. 2-6(a). We can see that the small signal gain of all the three channels are larger than 25 dB when the pump power of the LP_{11} mode is larger than 140 mW. At the absorbed pump power of 157 mW, the gain of the three channels are 26.6 dB, 26.1 dB and 26.9 dB, respectively. The gain difference between the three channels are always less than 1 dB. When the pump power exceeds 170 mW, the system starts lasing because there is a cavity formed between the DM and the end of the FMF inside the FM-WDM. To suppress this effect, we can add an AR coating on the FMF end.
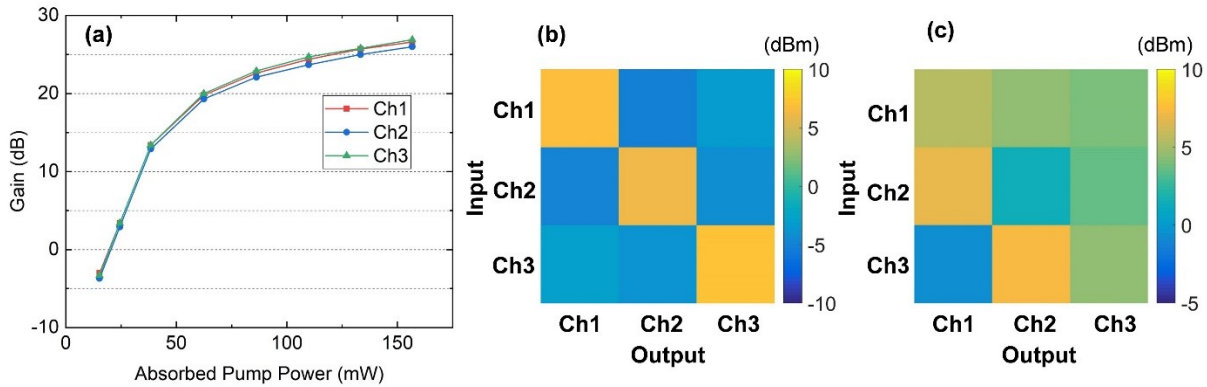
Figure 2-6: Experimental results (a) small signal gain of each channel vs. pump power, (b) transfer matrix of the FM-EDFA with retro-reflection at a pump power of 157mW, (c) transfer matrix of a pair of 3-mode symmetric PL.

We fixed the pump power at 157 mW, and measured the transfer matrix of the retro-reflecting amplifier. To measure the crosstalk matrix, we launched the small signal into one channel, and use three power meters to measure the output power of three output ports

simultaneously. Then did the same measurement for the other two channels to create the transfer matrix. The result is shown in Fig. 2-6(b). As can be seen, the matrix is nearly diagonal, the crosstalks of all three spatial channels are between -10 dB to -15 dB. In comparison, we also measured the transfer matrix of a pair of 3-mode symmetric PL without retro-reflection. The result is shown in Fig. 2-6(c). There is no obvious one-to-one relationship observed, the selectivity are no more than 3 dB for all the channels. One of the reasons for the residual crosstalk in the retro-reflecting FM-EDFA is the phase difference between the two mode groups is hard to be manually adjusted. The other reason comes from the mode mismatch between the passive and active FMF at the splice point, which will affect the total transfer matrix of the amplifier system. Both are not fundamental problems and can be improved in the future by using electronic feedback control of the stretcher and core size matched ED-FMFs. The mode-dependent loss of the PL is another reason for the crosstalks. The coupling loss of the reflected signal from DM into ED-FMF doesn't affect the crosstalk matrix. This is equivalent to insert a diagonal matrix between G^T and G in Eq. (2-1). As long as the values of this diagonal matrix are nearly equal, it will not introduce additional crosstalk.

We also swept the input signal wavelength across the C-band, and measured the gain and noise figure (NF) for the three channels. The pump power was fixed at 157 mW. The measured gain figure is shown in Fig. 2-7(a). We can see that the gain of all the three channels are greater than 25 dB for the signal wavelength ranges from 1530 nm to 1560 nm. The highest gain appears at 1530 nm, where the net gain for each channel are 30.3 dB, 29.6 dB, and 30.2 dB, respectively. Figure 2-7(b) shows the NF of the FM-EDFA. The NF looks flat across the C-band, ranging between 7 dB to 9.4 dB for all three channels. The coupling loss for the signal reflected from the

DM coupled into the ED-FMF before the second stage of amplification caused the NF to be slightly higher. In order to further improve the NF, we can either optimize the coupling of the reflected signal, or increase the pump power, to let the amplifier working at pump undepleted region.
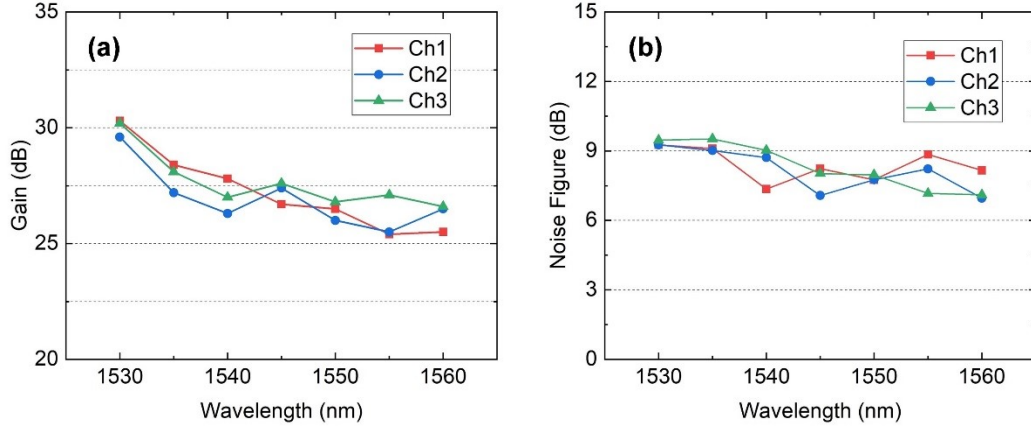
Figure 2-7: Measured (a) gain figure and (b) noise figure for each channel at different input signal wavelength across the C-band.

2.4 Fiber Design with Larger Low-Crosstalk Bandwidth

It is important to make sure the low-crosstalk feature can be achieved for a wide bandwidth, so that our amplifier system is compatible with wavelength-division multiplexing. In that case, the phase difference between LP modes inside the ED-FMF should keep constant at different input signal wavelengths. From Eq. (2-4) we can find that in order to satisfy this condition, the effective index difference Δn_{eff} must increases linearly with λ. We designed an ED-FMF with graded-index profile, as shown in Fig. 2-8(a), that can satisfy the above features [58]. It has a parabolic index profiles with a core radius of 14 μm, and the NA is 0.129, ensuring it supports two mode groups at entire C-band. We calculated the effective indexes of the first two LP modes of this fiber at each wavelength across the C-band, as shown in Fig. 2-8(b). We can see the effective indexes

of both LP modes are decreasing as the wavelength increasing, but the index difference is slightly

increasing. We further calculated the phase difference between the two LP modes across the C-

band, the result is shown in Fig. 2-8(c). As we can see, the change of $\Delta\varphi$ is very small and its value

is confined within $\pm\pi/10$ for almost entire C-band, which corresponding to the channel crosstalk

less than -10 dB. That means once the phase relationship is aligned well, one can change the input

signal wavelength without any other adjustments.
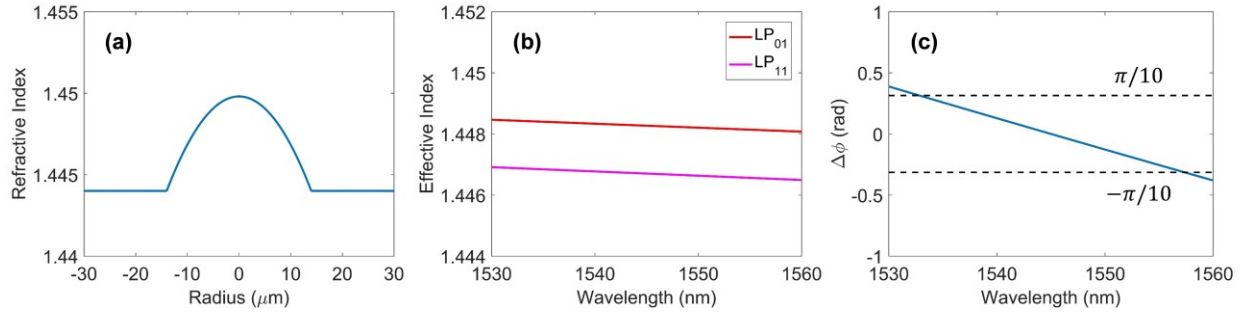
Figure 2-8: Designed refractive index profile of the graded-index ED-FMF with large low-crosstalk bandwidth, (b) calculated effective indexes of the two lowest LP modes, (c) phase difference between the first two mode groups across the C-band.

To design such a fiber that supports 3 mode groups, the power-law refractive index profile

can be optimized to make Δn_{eff} between successive mode groups the same. This design will scale

the operation of the proposed amplifier to six channels (spatial modes) when using a 6-to-1

symmetric PL. For fibers supporting more than three mode groups, special shapes of fiber

refractive index profile are needed to minimize the phase differences between mode groups.

CHAPTER 3   EDFA FOR OAM MODES USING AN ANNULAR-CORE PHOTONIC LANTERN

3.1 Introduction

Vortex beams carrying OAM associated with helical phase fronts [59] have been investigated intensely in the past few decades. These special types of laser modes can be useful in various applications. In microscopy, a vortex beam can enhance the resolution of images by orders of magnitude for a variety of structures [60, 61]. They can also be used to optimize the size of dark focal spots in stimulated emission depletion (STED) microscopy [62]. In material processing, high-order OAM beams can achieve clearer and smoother processed surfaces on a submicron scale [11, 63]. In addition, OAM modes can be used for high-precision optical measurements, such as the detection of a spinning object [64]. Recently, amplifiers for OAM modes have received significant interest since they are essential for high-power laser-related situations. EDFA for OAM modes has been studied theoretically [65], and an EDFA for the OAM$_{|L|=1}$ mode using phase plate based mode multiplexers has recently been validated experimentally [66]. However, phase plate based mode multiplexers are not ideal for this application, as they exhibit an appreciable coupling loss between free space and the amplifier fiber.

In this work, we demonstrate an EDFA for OAM modes using an annular-core photonic lantern. Since the photonic lantern (PL) is a low-loss all-fiber device, it can reduce coupling losses effectively and allows scaling to a larger number of OAM modes. In our experiment, both the first- and second-order OAM modes were amplified with small-signal gains of up to 22.1dB and 16.7dB, respectively, and the amplified OAM mode intensity profiles were captured by a CCD camera. We

17

also swept the signal wavelength through the C-band, and the results indicated that our scheme works well for the entire C-band.

3.2 Operational Principle
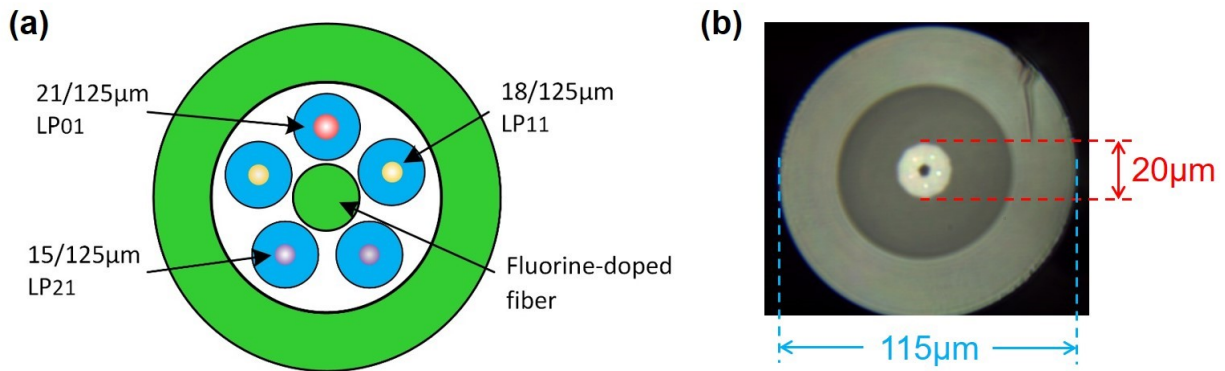
Figure 3-1: (a) Schematic cross-sectional view of the annular-core PL; (b) cross-section microscopic image of the fabricated annular-core PL.

In this experiment, we used an annular-core PL to generate the OAM modes efficiently in a low-loss fashion [67]. Fig. 3-1(a) shows the structure of the input cross-section of this PL. It contains five single-mode input fibers of dissimilar size inside a low refractive index capillary and a pure fluorine-doped central fiber. During adiabatic tapering, each input fundamental mode can evolve into a specific LP mode at the output. The input fiber cladding forms the core area at the output of the PL, which has an annular shape. The cross-sectional image at the output is shown in Fig. 3-1(b), which depicts a ring core with a thickness of 8μm and cladding with a diameter of 115μm.
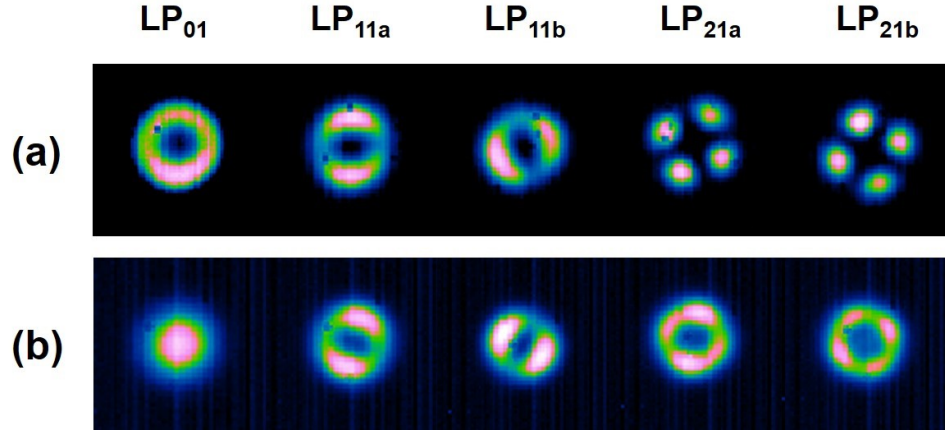
Figure 3-2: Measured mode intensity profile using an SLD with a center wavelength of 1550 nm (a) at the output of the ring-core PL, and (b) after splicing with a 1-meter 6-LP mode FMF.

We employed a super luminescent diode (SLD) with a center wavelength of 1550 nm and launched it into each input SMF, then measured the mode intensity profiles at the output of the annular-core PL. The results are shown in Fig. 3-2(a). As can be seen, the first five LP modes were generated successfully. The LP_{01} mode has a donut-shaped beam profile but does not carry OAM. Next, we spliced the PL with a 1-meter length of 6-LP mode FMF, whose core and cladding diameters were16 and 125 μm, respectively. We also measured the output mode profiles from the passive FMF, which are shown in Fig. 3-2(b). Once transmitted into the FMF, the LP_{01} mode reverted back to its Gaussian-shaped mode profile, while the other LP modes' beam profiles maintained their shapes well.

The scalar OAM modes in the optical fiber can be expressed as superpositions of two degenerate LP modes with 90-degree phase differences. For example, the $OAM_{|L|=1}$ with a donut-shaped intensity distribution and a spiral phase profile could be created by launching two degenerate LP_{11} modes with a 90-degree phase difference simultaneously, as shown in Fig. 3-3(a). Similarly, the $OAM_{|L|=2}$ mode could be generated by using two degenerate LP_{21} modes, as shown

in Fig. 3-3(b). Since our PL can multiplex both degenerate LP$_{11}$ modes and LP$_{21}$ modes, by adjusting the phase delay between the two input SMFs carefully, it should be possible to generate both OAM$_{|L|=1}$ and OAM$_{|L|=2}$ modes at its output.
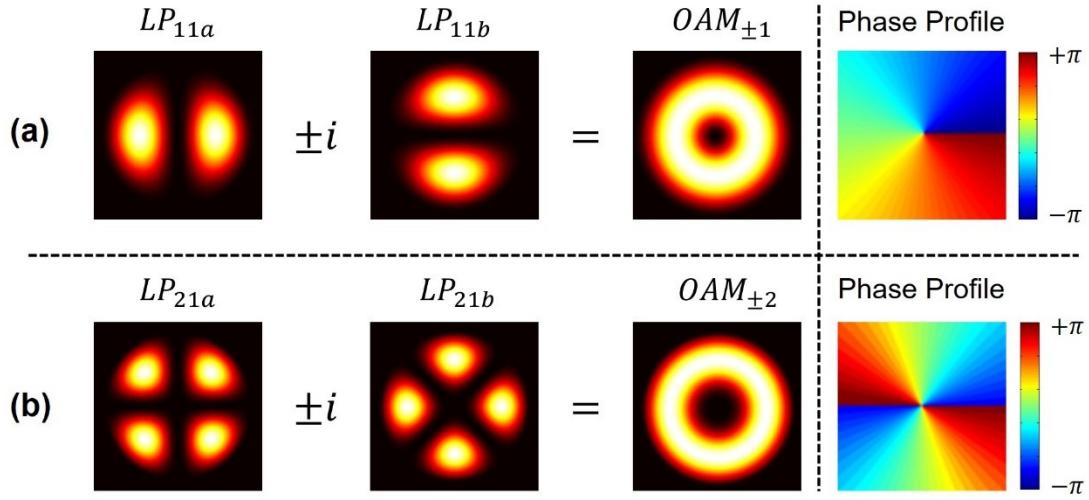
Figure 3-3: Demonstration of the generation of OAM modes in fiber via the superposition of two degenerate LP modes for (a) OAM$_{|L|=1}$, and (b) OAM$_{|L|=2}$.

3.3 Experimental Setup
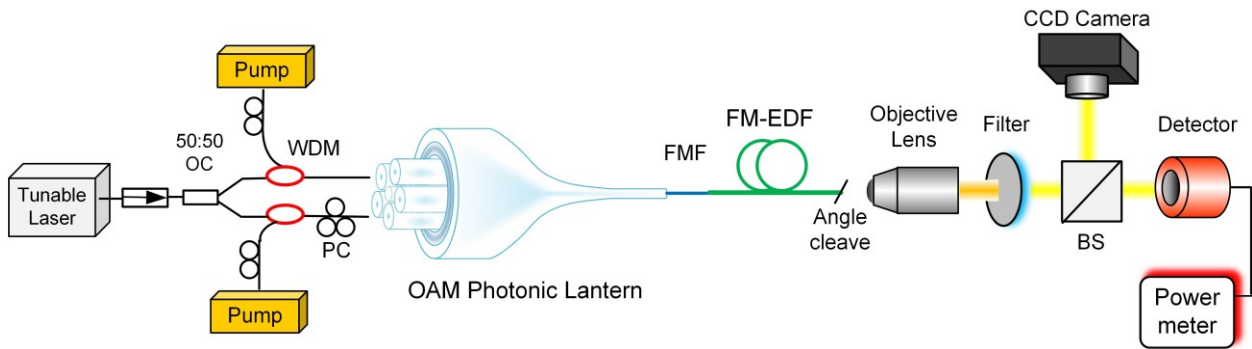
Figure 3-4: Experimental setup of the OAM EDFA based on the annular-core PL. OC: optical coupler; PC: polarization controller; BS: beam splitter.

The experimental setup of our OAM EDFA is shown in Fig. 3-4. The signal laser was launched from a tunable laser with an optical power of 0.2 mW at 1550 nm. After it was split into

two channels by a 3-dB optical coupler, each channel was combined with the 967 nm pump by a WDM coupler. The output of one of the two WDMs can be connected to either the $LP_{11a,b}$ or $LP_{21a,b}$ port of the ring-core PL to generate the $OAM_{|L|=1}$ and $OAM_{|L|=2}$ modes. Before the PL, a polarization controller (PC) was used to make sure the two degenerate modes were polarized in the same direction and that their phase difference was $\pm\pi/2$. The output of the PL was spliced with a 1-m-long intermediate 6-LP FMF and further spliced with a 5-m-long erbium-doped FMF (ED-FMF). The gain fiber had core and cladding diameters of 13 and 163μm, respective, possibly supporting over 6 LP modes at the signal wavelength. The amplified signal was focused by an objective lens, and a bandpass filter centered at 1550nm was employed to block the residual pump light. The amplified OAM signal power was detected by a power meter, and their mode profiles were captured by a CCD camera.

3.4 Experimental Results and Discussion
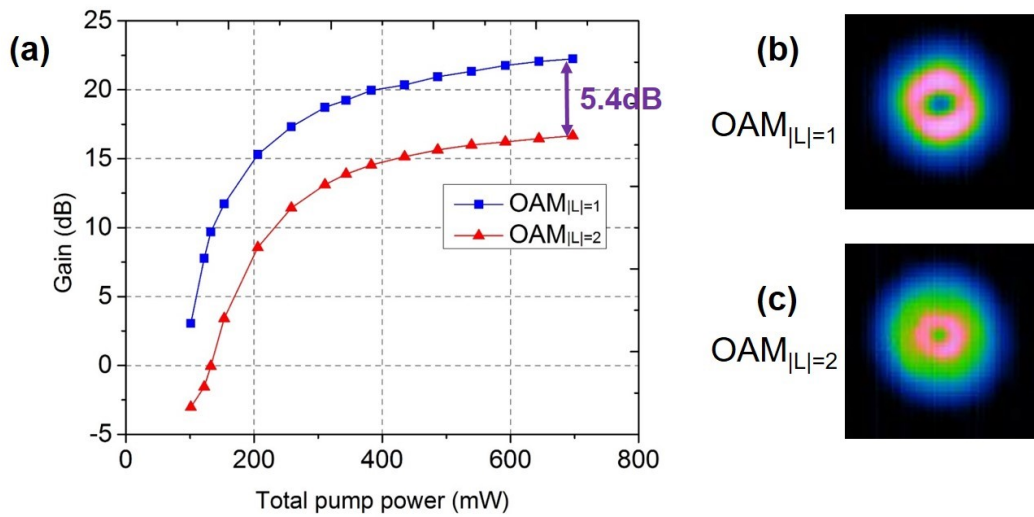
Figure 3-5: (a) Small signal gain of $OAM_{|L|=1,2}$ vs. total pump power; mode intensity profiles of the amplified (b) $OAM_{|L|=1}$ and (c) $OAM_{|L|=2}$ modes.

Fig. 3-5(a) shows the signal gain figure of $OAM_{|L|=1,2}$ under different pump powers (LP_{11a+b} or LP_{21a+b}). When the total incident pump power at the input of the PL was 697 mW, the small signal gain for $OAM_{|L|=1}$ and $OAM_{|L|=2}$ were 22.1dB and 16.7dB, respectively. The differential modal gain (DMG) was 5.4 dB. The gain for $OAM_{|L|=2}$ was smaller than that for $OAM_{|L|=1}$ mainly due to the insertion loss of the PL for LP_{21} modes, which are larger than LP_{11} modes at both the pump and signal wavelengths. We used a CCD camera the capture the mode profiles of the two OAM modes after amplification, and the results are shown in fig. 3-5(b) and (c). We can see that both of them have doughnut-shaped intensity profiles, which indicates that they are vortex beams after amplification. However, the patterns seem to be less than perfectly symmetric, which is partly due to an imperfect gain equalization between two degenerate LP modes. The main reason for the lack of symmetry is that there is mode crosstalk in the gain fiber, meaning that the original LP modes will couple to higher-order modes supported by the gain fiber and undergo further amplification.
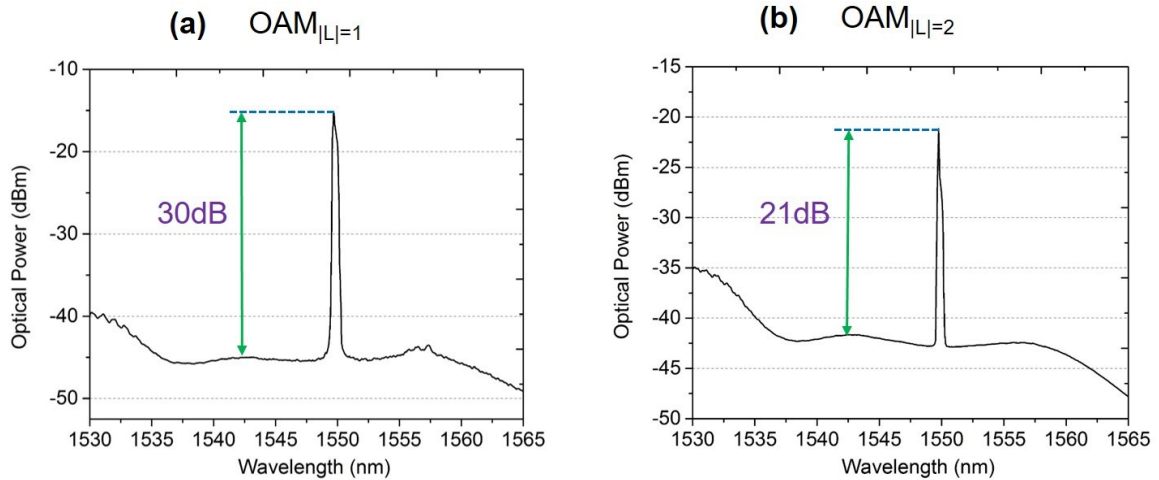
Figure 3-6: Measured optical spectra for the amplified OAM signals: (a) $OAM_{|L|=1}$ and (b) $OAM_{|L|=2}$ modes.

We fixed the pump power as 592 mW and measured the optical spectra of the amplified signals; the results are shown in Fig. 3-6. After amplification, the resulting optical signal-to-noise ratio (OSNR) of the $OAM_{|L|=1}$ mode was 30 dB, which is 11 dB lower than the input signal from the tunable laser. The OSNR of the $OAM_{|L|=2}$ mode was 21 dB, which is 20 dB lower than the input signal. The lower OSNR of the amplified $OAM_{|L|=2}$ signal was mainly caused by the higher mode-dependent loss (MDL) of the PL for the LP21 modes. We also find that the ASE noise level of the $OAM_{|L|=2}$ mode was higher than that of the $OAM_{|L|=1}$ mode.
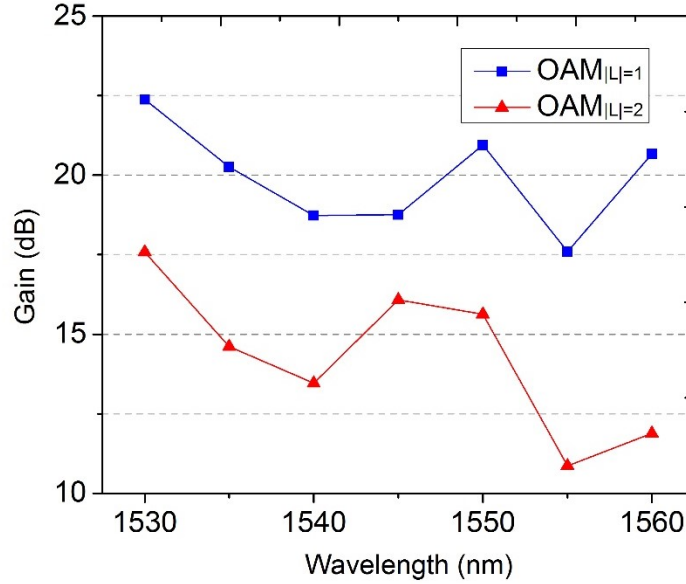
Figure 3-7: Gains figures of the two orders of OAM modes at different signal wavelengths.

Finally, we fixed the total pump power as 486 mW and swept the input signal laser wavelength from 1530 nm to 1560 nm; the results are shown in fig. 3-7. We found that the gain curves for both $OAM_{|L|=1}$ and $OAM_{|L|=2}$ were similar to the ASE spectrum for the gain media. The minimum DMG of just 2.7 dB was achieved at 1545 nm.

CHAPTER 4   TRANSVERSE MODE-SWITCHABLE ERBIUM-DOPED FIBER LASER

4.1 Principle and Key Components

In this work, we used mode-selective photonic lantern (MSPL) to realize the transverse mode conversion between the fundamental mode in the SMF and HOMs in the FMF. In general, MSPLs are passive all-fiber devices capable of efficiently multiplexing single-mode inputs and converting each input into a specific LP mode. Among other applications, the PL has great potential for SDM systems [68, 69], as well as spatial mode control for high power fiber amplifiers [39]. In general, a PL consist of a set of SMFs inserted into a capillary tube whose index of refraction is lower than the refractive index of the SMF cladding. The tube is adiabatically tapered down to create an FMF output at the taper waist [56], as shown in Fig. 4-1(a). The mode selectivity feature can be obtained if the input SMF core sizes are different. Each input fundamental mode evolves into a particular mode at the output FMF with a matched propagation constant [55, 70]. For a 6-mode MSPL, its input facet contains 6 graded-index fibers with core diameters of 23, 18, 18, 15, 15, and 11μm, which map to the LP_{01}, LP_{11a}, LP_{11b}, LP_{21a}, LP_{21b}, and LP_{02} mode, respectively [57]. After tapering, the resulting FMF's cladding diameter is 110 μm while the core diameter is 20 μm. The microscope image of the cross section of the output FMF is shown in Fig. 4-1(b). The refractive index contrast of the core and the fluorine-doped silica capillary is $\Delta n = 9.5 \times 10^{-3}$. The output facet of the PL can be easily spliced with a 6-mode FMF, which has a core and cladding diameter of 16/125 μm. The mode profiles at the output of the spliced FMF were measured at 1550 nm and are shown in Fig. 4-1(c). We can clearly see that the six lowest order LP modes are well preserved after they propagate through the FMF.
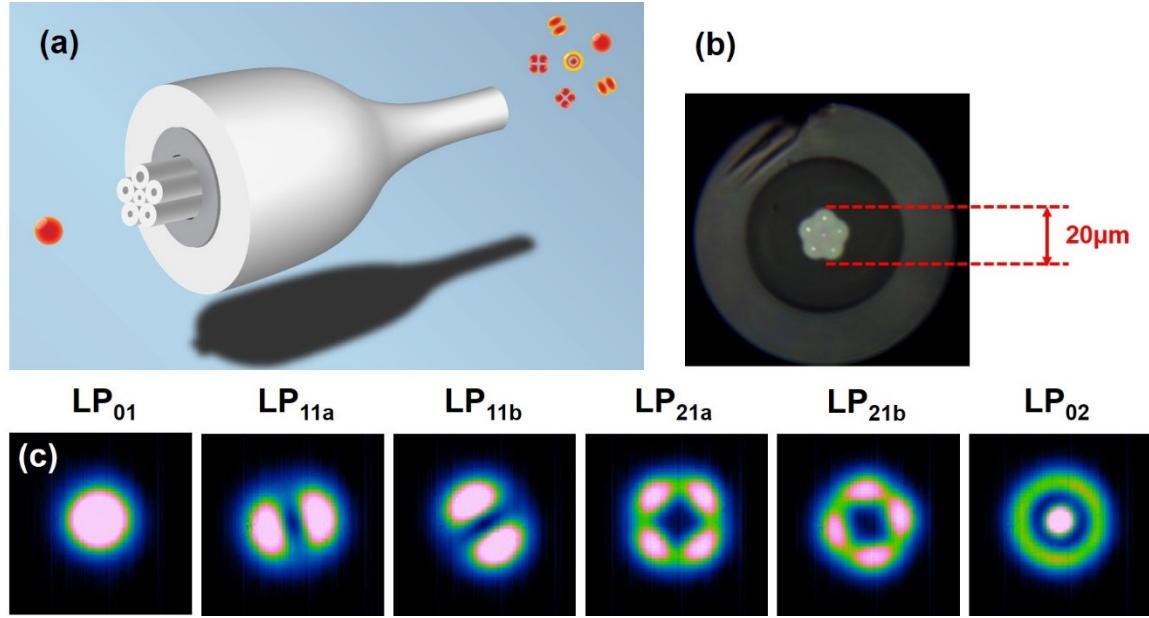
Figure 4-1: (a) Schematic of a 6-mode MSPL; (b) cross-sectional microscope image of the output of the MSPL; (c) mode profiles of the MSPL after splicing to a 6-mode FMF at 1550 nm.

The fabricated MSPL has mode-dependent losses (MDL) as a consequence of imperfections in the PL taper. The total losses of the PL (including insertion loss and splice loss) for both pump and signal wavelength were measured, the results are shown in Table 4-1. We found the loss for the LP_{02} mode was larger than for other LP modes at both wavelengths.

Table 4-1. Losses of the MSPL at both pump and signal wavelength (in dB)

	LP_{01}	LP_{11a}	LP_{11b}	LP_{21a}	LP_{21b}	LP_{02}
976 nm	0.88	1.66	0.55	0.98	0.96	2.97
1550 nm	1.71	3.75	1.79	2.29	1.46	4.35

The gain media used in this experiment was an ED-FMF which was fabricated in house [35]. Figure 4-2(a) shows the measured refractive index profile of this fiber, and Fig. 4-2(b) shows the microscope image of this ED-FMF cross section. The core and cladding diameters of the ED-FMF are 13 μm and 163 μm, respectively, with a step-index profile. The estimated numerical

aperture (NA) was 0.249, ensuring that more than 6 LP modes were supported at $\lambda = 1550$ nm. The core area was uniformly doped with pure erbium ions at a dopant density of 4.5×10^{25} m^{-3}, which supports a maximum gain of nearly 10 dB/m for each spatial mode at 1550 nm. We spliced the ED-FMF with the passive 6-mode FMF and measured the mode profile of each LP mode at the output, the results are shown in Fig. 4-2(c). We can see that the higher-order modes (LP$_{21}$ and LP$_{02}$) are slightly distorted due to the core size mismatch.
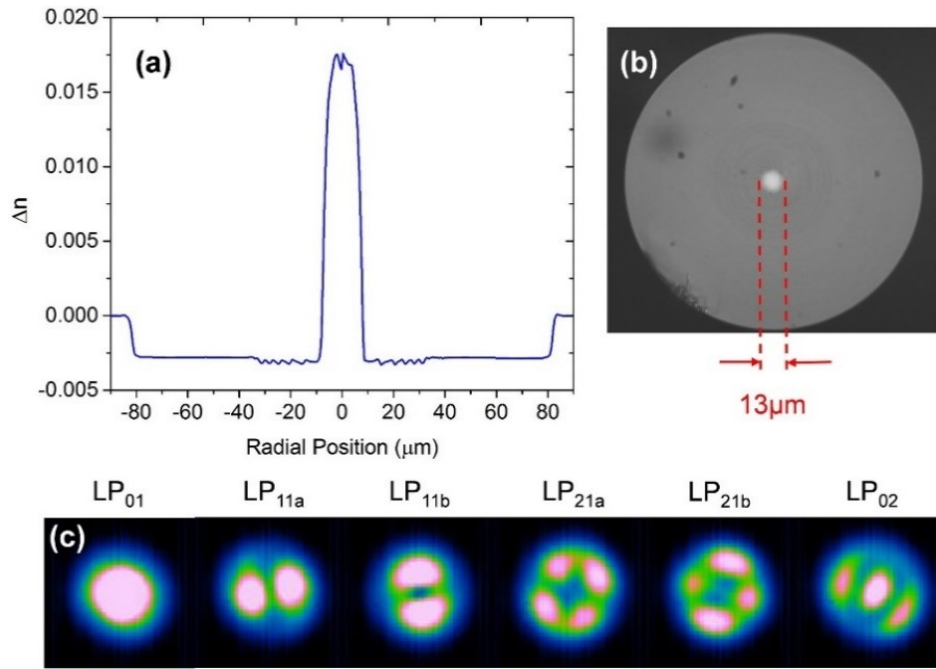
Figure 4-2: (a) Measured refractive index of the ED-FMF; (b) cross-sectional image of the ED-FMF; (c) mode profiles from ED-FMF spliced with 6-mode FMF.

4.2 Experimental Setup and Results

4.2.1 LP Modes Switchable Laser
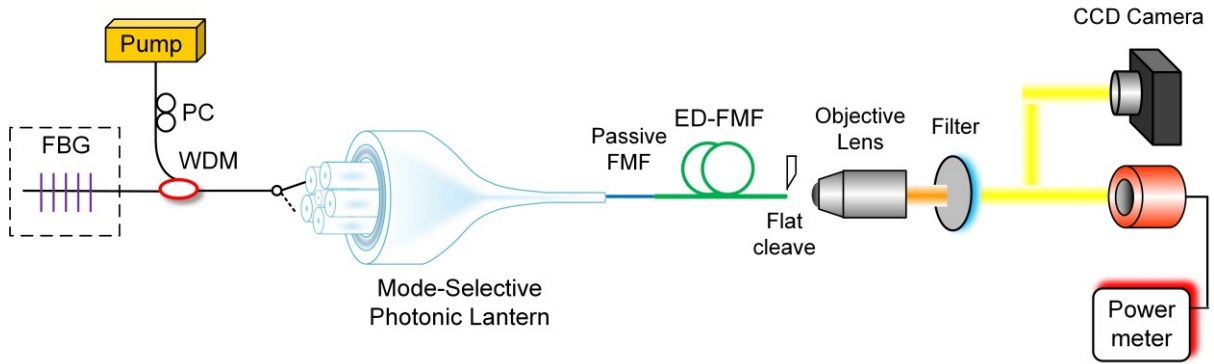
Figure 4-3: Experimental setup for the transverse mode-switchable fiber laser. PC: polarization controller; FBG: fiber Bragg grating.

Figure 4-3 shows the experimental setup of the mode-switchable fiber laser. Light from the pump diode (pigtail fiber type: SM98-PS-U25A) with a central wavelength of 976 nm travels through a polarization controller (PC) to optimize the injected power. After the PC was a WDM coupler (fiber type: HI1060 FLEX). The other input port of the WDM was connected to a fiber Bragg grating (FBG) with a central wavelength of 1536.8 nm and a reflection bandwidth of 0.6 nm. The FBG was made of standard SMF, the reflectivity of the FBG was measured as 60%. In order to generate the desired laser mode, the output of the WDM could be switched to any one of the six input SMFs of the PL. On the other side, the output of the PL was first spliced to a 1-meter passive 6-mode FMF, which was then spliced to a 5 m long ED-FMF. The intermediate passive FMF reduced the splicing loss that would occur between the PL and gain fiber due to the mismatch in their core sizes. The end of the ED-FMF was cleaved to be flat, yielding a 4% Fresnel reflection

27

coefficient. The laser cavity was formed between the FBG and the end of EDF. Within each round trip, only one specific LP mode can pass through the lantern and be amplified. Hence, it should be noted that our pump and signal are the same mode which is beneficial for maximizing the amplifier gain. The laser output was focused using a 20X objective lens, and a band-pass filter at 1540 nm with a full-width half-maximum bandwidth of 12 nm was placed right after the lens to block the residual pump light. We measured the laser output power using a power meter, and the laser mode profiles using a CCD camera.
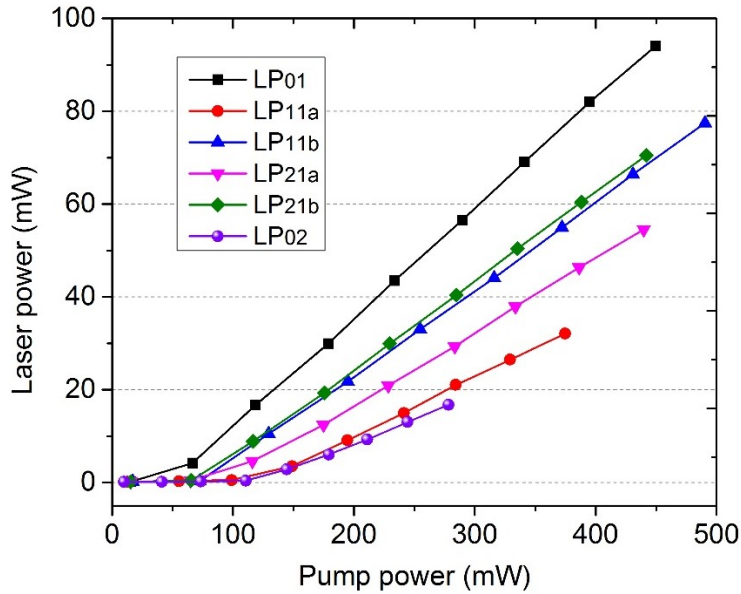
Figure 4-4: Output power vs. pump power for the six lasing modes.

The measured output laser powers versus pump power for all 6 lasing modes are shown in Fig. 4-4. The horizontal axis shows the pump power measured at the passive FMF output. It should be noted that there are splicing losses between the passive FMF and the gain fiber, and the losses are different for each LP mode, so the absorbed pump powers are smaller than the values shown in Fig. 4-4 and are not the same for all the pump modes. From Fig. 4-4, we can see that all six LP

modes can lase when the pump power surpasses their threshold. The LP_{01} lasing mode has the highest output power at >90 mW, with a slope efficiency of 23.6%. The slope efficiencies for LP_{11a}, LP_{11b}, LP_{21a}, LP_{21b} and LP_{02} lasing modes are 12.8%, 18.7%, 16%, 19.2%, and 10.9%, respectively. The difference in slope efficiencies and threshold values are mainly due to the MDL of the PL at the signal wavelength and different overlap integrals between the pump and signal mode intensity profiles. In order to increase the slope efficiency, a FBG with higher reflectivity or a lower-loss MSPL, to reduce round trip loss, can be used. To decrease the threshold pump power, the EDF output can be angle cleaved and an output coupler with high reflectivity can be added to the end of the gain fiber to further reduce cavity loss.
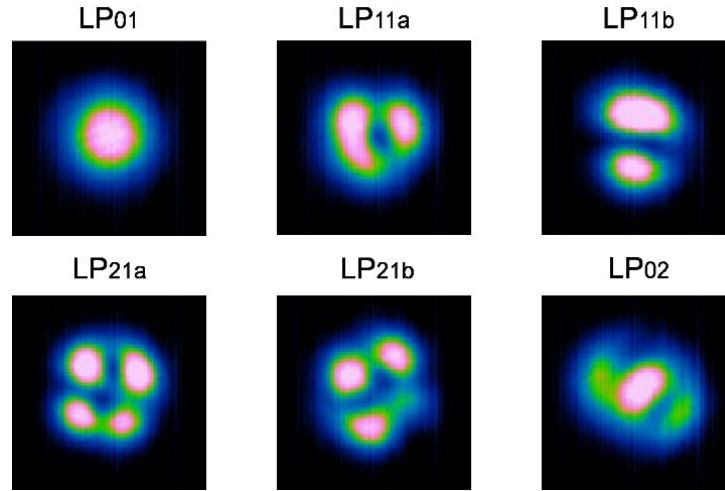
Figure 4-5: Intensity profiles of the six lasing LP modes.

In order to the obtained mode profiles, we fixed the laser power of each lasing mode to be 15 mW, and used a CCD camera (Xenics Xeva-1.7-320) to capture their mode intensity profiles. Two attenuators were used in front of the CCD camera to prevent saturation. The camera images of the mode intensity profiles are shown in Fig. 4-5. It is important to highlight that all six laser mode patterns do not suffer greater distortions during the lasing operation, compare to Fig. 4-2(c).

For the five lowest-order (LP_{01}, LP_{11s} and LP_{21s}) lasing modes, their profiles are almost ideal, but slightly distorted. This was likely due to mode crosstalk of the PL, leading to some of the single-mode input ports exciting multiple modes in the ED-FMF. Another reason could be residual mode coupling within the ED-FMF. For the LP_{02} mode, its mode profile does not look as well. This is mainly due to the core size mismatch at the splice between the passive FMF and ED-FMF. The mode profile will be distorted after propagating in the ED-FMF, as shown in Fig. 4-2(c). When propagated through the gain fiber, the mode profile will degrade compared to the result in the passive FMF. This problem can be fixed by using an ED-FMF whose core size better matches the 6-mode FMF core size. The mode profiles of the six LP modes didn't change as laser power increased, and were stable at room temperature. It is worth mentioning that even higher-order lasing modes could be generated if the 6-mode MSPL was replaced by a 10-mode or 15-mode MSPL [71].
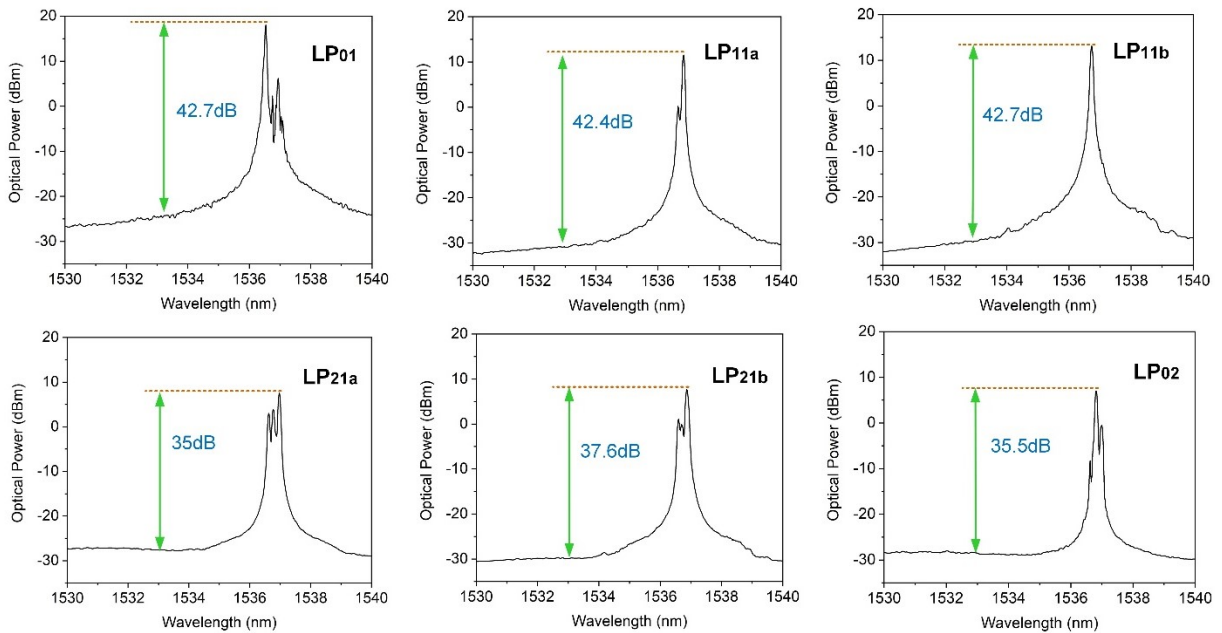
Figure 4-6: Output optical spectra of the six lasing modes measured by an OSA with a resolution of 0.1 nm.

30

In the following, we measured the optical spectra of the output lasing modes using an OSA with a 50/125 μm graded-index optical fiber input port (Ando AQ-6315e), capable of accepting high-order modes. By inserting the end of ED-FMF into a bare fiber adapter and further connecting to the input port of the OSA, we can observe the optical spectrum of each laser mode, as shown in Fig. 4-6. The resolution of the OSA was set to be 0.1 nm. The pump power was fixed at 484 mW. According to Fig. 4-6, we find that all six modes have a central wavelength near 1537 nm and a bandwidth less than 1 nm. This matches well with the reflection spectrum of the FBG. It also indicates that the OSNR for all six lasing modes was above 35 dB, ranging from 35 dB to 42.7 dB. Note for some modes, there were multiple longitudinal modes are observed. There were several sidebands apart from the main peak. These sidebands are believed to be caused by the mode crosstalk of the MSPL. When the gain is high enough, the modes produced by crosstalk of the MSPL can also lase. Since different LP modes have different effective indices in the ED-FMF, they may lase at slightly different wavelengths within the reflection bandwidth of FBG, with a lower peak power compared to the selected LP mode.

4.2.2 Donut-Shaped Mode Lasers
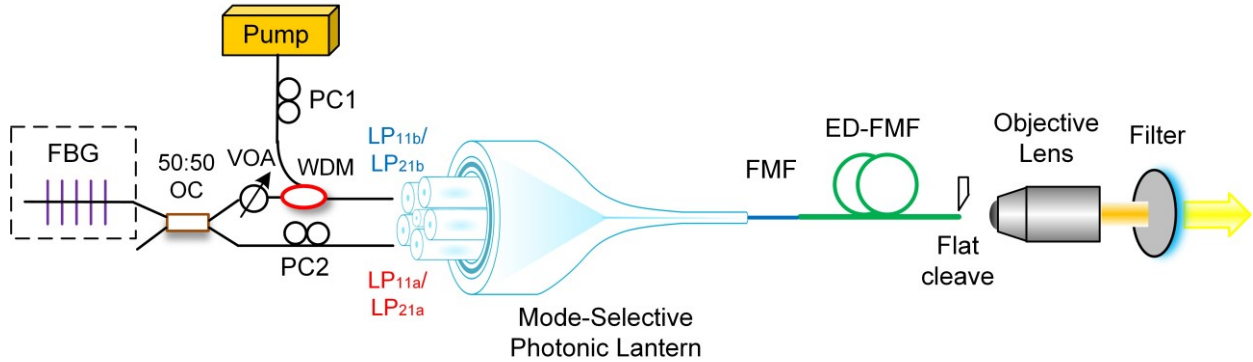
Figure 4-7: Schematic of a fiber laser for the generation of donut-shaped modes by the incoherent superposition of degenerate LP_{11s} or LP_{21s} modes. OC: optical coupler; VOA: variable optical attenuator.

Now, we focus on obtaining a donut-shaped mode profile laser. Laser emission with a donut-shaped mode profile was generated by the incoherent superposition of two degenerate LP modes. The experimental setup used to obtain this type of fiber laser is shown in Fig. 4-7, only the SMF side was modified compared to the setup for generating LP modes. When the light was reflected back from the FBG, it was split into two arms by a 3-dB optical coupler (OC). The upper arm went through a variable optical attenuator (VOA) that then connected to the signal port of the WDM. The output of WDM was then connected to either the LP_{11b} or LP_{21b} input port of the PL, and the lower arm of the OC was connected to the corresponding LP_{11a} or LP_{21a} port of the PL. When the upper channel is pumped, both channels can lase together with the same gain media. Since the two lasing modes go through different cavities, the output laser could be an incoherent superposition of the two degenerate modes. We adjusted PC2 to ensure the orientation of the two degenerate modes are orthogonal with respect to each other. Thus the superposition of the two degenerate LP modes is a donut-shaped mode. Both donut LP_{11} and LP_{21} modes were generated

using our setup. It should be noticed that a VOA was employed to adjust the laser power between the two lasing modes. Otherwise, the laser power of the two modes could be different and would cause the output mode profile to be non-circularly symmetric. Using the same band pass filter to block the pump light, we measured both the laser power and the mode intensity profiles.
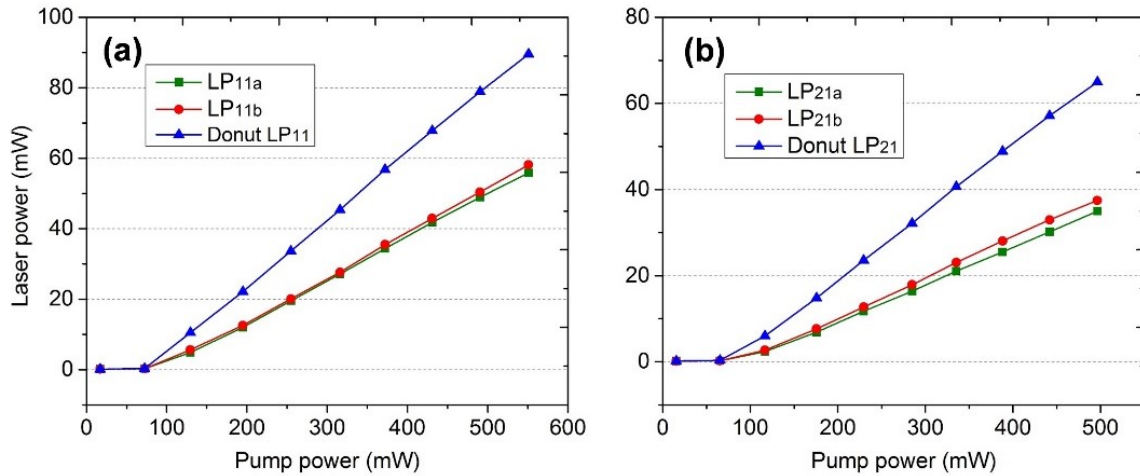
Figure 4-8: Laser power vs pump power for each LP mode lasing separately and the donut mode as their incoherent superposition for the (a) LP_{11} modes and (b) LP_{21} modes.

First, we measured the laser power of each degenerate LP mode separately. We disconnected the signal port of the WDM coupler to measure the laser power of LP_{11a} mode. Then, we disconnected the LP_{11a} port of the PL to measure the laser power of LP_{11b} mode. We gradually increased the attenuation of the VOA to make sure the laser power of the two modes were almost the same. Finally, both channels were connected to measure the result of the donut LP_{11} mode. The same measurements were performed for the LP_{21} modes. The results are shown in Fig. 4-8. The slope efficiency for the two degenerate LP_{11} modes were 12.4% and 12.8% and the result of the donut LP_{11} mode was 18.9%. The laser output power of the donut-shaped mode was 89.5 mW at a pump power of 551 mW. The slope efficiency of single LP_{21a} and LP_{21b} laser modes were 8.8%

and 9.4% and the slope for the donut LP_{21} mode was 15.7%. The laser output power of the donut LP_{21} mode was measured to be 65 mW when the pump power was 496 mW.

Compared to Fig. 4-4, we find that at the same pump power, the laser power of each LP mode lasing individually is smaller than the result in Fig. 4. This is due to the 3-dB coupler in the laser cavity, that for each round trip causes 6 dB of additional loss, which caused the decrease of the laser power. According to Fig. 4-8, the laser power of the donut mode was always smaller than the sum of two degenerate LP modes due to gain saturation.
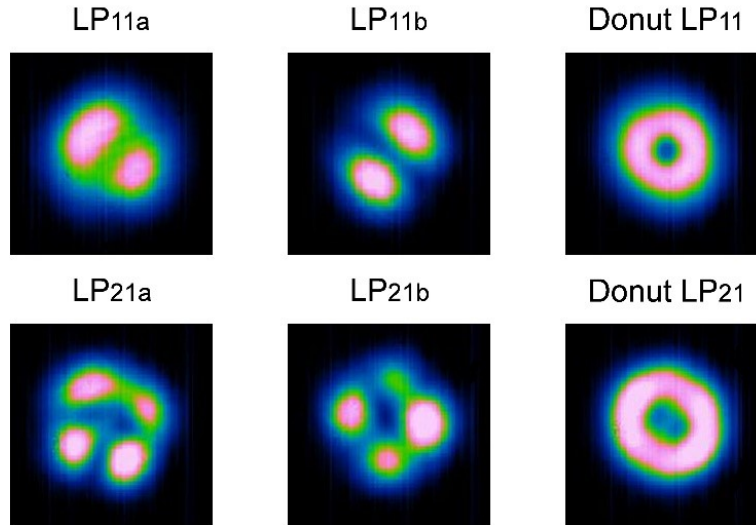
Figure 4-9: Measured mode profiles for each individual LP lasing mode and the donut LP mode comes from their incoherent superposition.

Coming back to the obtained mode profiles for the donut-shaped lasers, the results are shown in Fig. 4-9. The upper row shows the mode profiles of each LP_{11} mode lasing individually and their incoherent superposition, which is the donut LP_{11} mode. The lower row shows the results for each LP_{21} modes lasing separately, as well as the donut LP_{21} mode. The results of the four degenerate LP_{11s} and LP_{21s} mode are similar to the single LP laser mode results shown in Fig. 4-5. And when two degenerate LP modes lase together, the donut shaped laser mode profiles are clearly

observed. Both donut LP_{11} and LP_{21} modes have a circular mode intensity profile, as shown in Fig. 4-9. However, the donut modes are not perfectly symmetric. This is due to imperfections in the mode profiles of each degenerate LP mode.
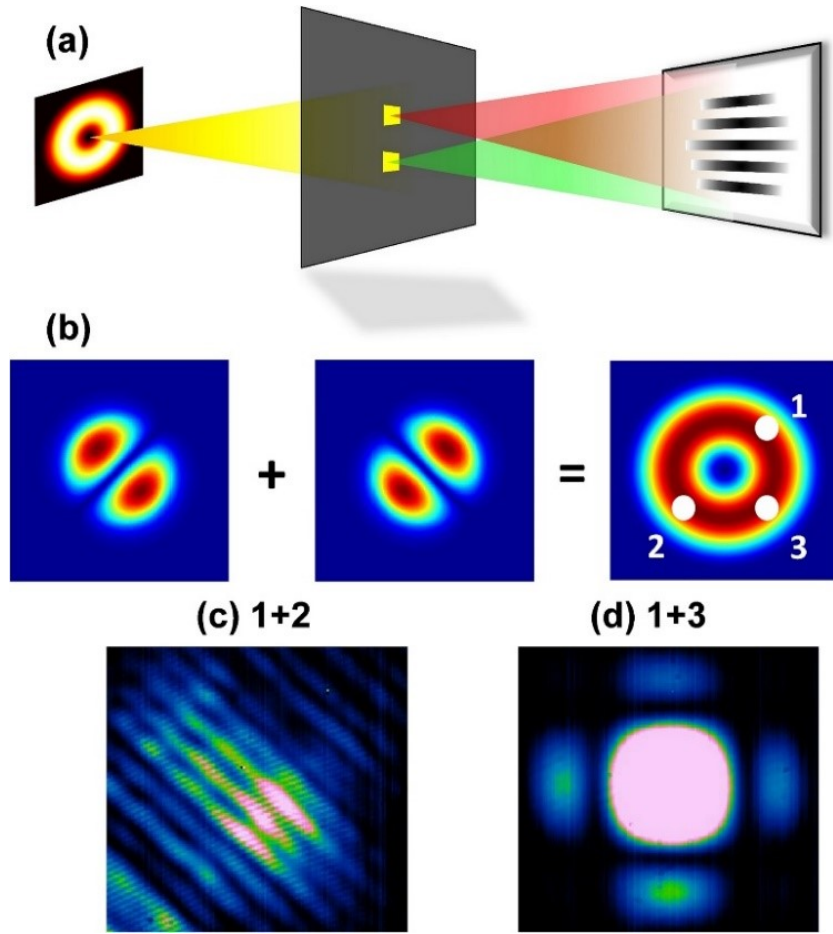
Figure 4-10: (a) Schematic setup of interference experiment to verify the incoherence of the donut mode laser; (b) position of the pinholes correspond to the lobes on the donut mode laser; and the interference patterns between points 1 and 2 (c) and points 1 and 3 (d).

To verify the incoherence of the donut mode laser, we conducted an interference experiment. Its working principle was described in [28]. The donut LP_{11} mode was selected for demonstration purposes because it can be easily observed due to its larger pedal size. Figure 4-10(a) shows a schematic of the setup for the interference experiment. We let the donut beam passed

through a double pinhole, and the resulted interference pattern was observed on the camera screen. The shape of the pinholes was square. The position of the pinholes corresponded to the lobes of the donut mode laser as depicted in Fig. 4-10(b). When points 1 and 2 are interfered, because they come from the same LP_{11} mode, strong fringes should be observed. However, when points 1 and 3 are interfered, because they are generated by two incoherent source, we are supposed to see no interference fringes.

The interference result of points 1 and 2 is shown in Fig. 4-10(c). Strong fringes can clearly be seen, as was expected. Conversely, no fringes can be seen when interfering points 1 and 3, as shown in Fig. 4-10(d). The fringes on the edge of the pattern in Fig. 4-10(d) are the diffraction pattern from the square shaped pinhole, which is a sinc function in two-dimensional, not from interference between two beams.

CHAPTER 5   MODE-SELECTIVE FEW-MODE BRILLOUIN FIBER LASERS

5.1 Introduction

Stimulated Brillouin scattering (SBS) is one of the prominent nonlinear effects in optical fibers. It can be described as a nonlinear interaction between the pump and Stokes wave mediated by the acoustic wave [72]. Brillouin fiber laser (BFL) could be realized in a fiber ring cavity by using SBS to provide gain for the signal travelling in the backward direction [73, 74]. There is a number of advantages of the BFLs. For example, the optical signal-to-noise ratio (OSNR) of a BFL is usually much higher than that of the pump laser due to the stronger damping of the acoustic field compared to the optical field [75, 76]. Also, BFLs has attracted interests due to their ultra-narrow linewidth [77, 78]. A BFL with a linewidth of tens of Hz has been experimentally demonstrated [79], which can be, in turn, used for high quality microwave signal generation [80, 81]. Based on cascaded SBS processes, multiple wavelengths laser sources could be generated in a single ring cavity [82, 83]. Recently, an LP_{01} and LP_{11} mode BFL based on only intra-modal SBS in the two-mode FMF has been reported [84]. However, intermodal SBS caused the degradation of laser mode purity.

In this work, we demonstrate, for the first time, an intra-cavity transverse mode-selective BFL based on intermodal SBS effect with the fundamental mode as the pump. A pair of MSPLs were placed inside the ring cavity to act as spatial mode filters. In this configuration, pump mode converters are not necessary. For comparison, we also generated the BFLs of the three lowest-order LP modes based on intra-modal SBS effect. The laser slope efficiencies, mode intensity profiles, optical spectra, and linewidths were characterized for both cases.

5.2 Working Principle
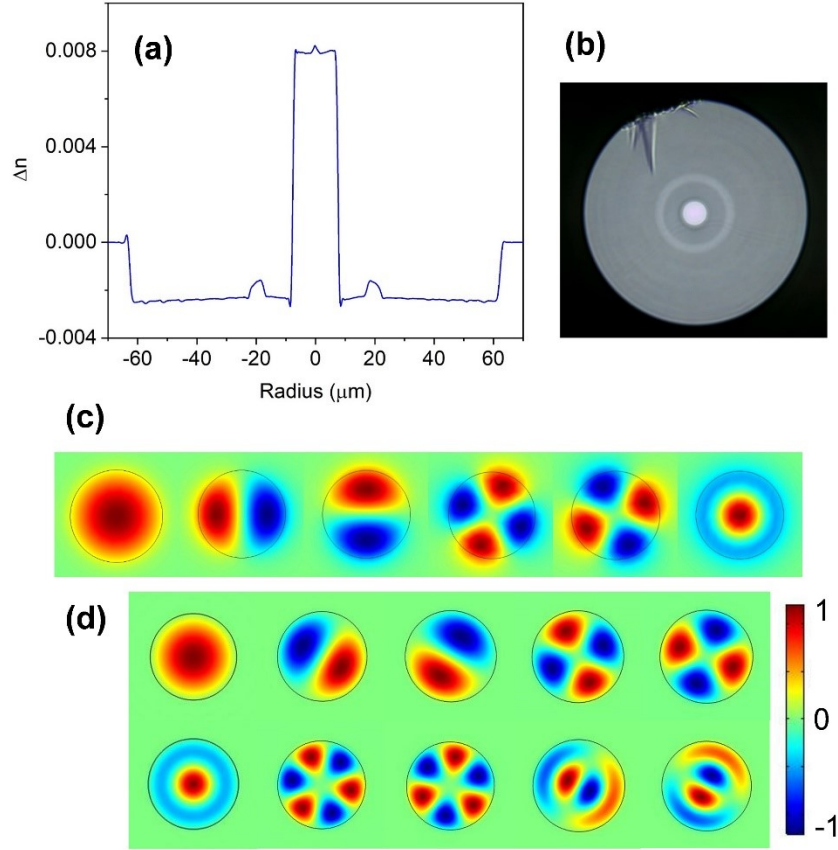
Figure 5-1: (a) Refractive index profile and (b) cross-sectional microscope image of the 4-LP mode FMF, (c) optical fields of the 6 LP modes, (d) field distributions of the 10 lowest order of guided acoustic modes.

The FMF used in our experiment is the 4-LP mode FMF made by Prysmian Group. Its refractive index profile is shown in Fig. 5-1(a), and its cross-sectional microscope image is shown in Fig. 5-1(b). It is a step-index fiber with a core and cladding diameter of 15.2 μm and 125 μm, respectively. The numerical aperture (NA) was measured to be 0.17, ensuring it supports 6 LP modes at a wavelength of 1550 nm. We calculated the transverse field distributions of the 6 LP modes supported by this FMF at 1550 nm by COMSOL, the results are shown in Fig. 5-1(c). We also computed the guided acoustic modes of the fiber at a frequency of 10.6 GHz, which is the

Brillouin frequency shift for the backward SBS. Figure 5-1(d) shows the material density vibration fields of the 10 lowest order of longitudinal acoustic modes guided in the core area. It should be noted that the number of guided acoustic modes of the same fiber is much larger than that of the optical modes [85].

Both intra-modal and intermodal SBS will occur in the FMF once the field distribution of the acoustic wave is matched with the pump and scattered Stokes waves. The Brillouin gain spectrum is essentially a combination of gain peaks generated by each guided acoustic modes [86]:

$$g(\Omega) = \sum_m g_{0m} \frac{(\frac{\Gamma_B}{2})^2}{(\Omega - \Omega_m)^2 + (\frac{\Gamma_B}{2})^2} \tag{5-1}$$

where Ω_m is the acoustic frequency of the m-th guided acoustic mode; Γ_B is the acoustic damping rate; g_{0m} is the gain coefficient created by the m-th acoustic mode, which is proportional to the square of the field overlap integral between the two optic fields and one acoustic field. The overlap integral can be expressed as:

$$\eta_{ijm} = \iint \varphi_{i,p} \xi_m \varphi_{j,s}^* \, ds \tag{5-2}$$

where $\varphi_{i,p}$ and $\varphi_{j,s}$ means the normalized field distribution of the i-th pump wave and j-th Stokes wave; and ξ_m is the normalized field distribution of the m-th guided acoustic mode. We found that the Brillouin gain coefficients mediated by the higher-order acoustic modes would be much smaller, because their higher spatial frequencies decrease the field overlap with the optic modes.

Table 5-1. Overlap integrals of normalized acoustic and optic fields that form the main Brillouin gain peaks.

	LP$_{01,s}$	LP$_{11,s}$	LP$_{21,s}$
LP$_{01,p}$	9.15×10^4	7.76×10^4	6.56×10^4
LP$_{11,p}$	--	7.15×10^4	--
LP$_{21,p}$	--	--	5.47×10^4

Here we calculated the value of η_{ijm} for different pump and Stokes wave pairs associate with the acoustic mode that provides the highest Brillouin gain, as shown in table 5-1. We can find that for HOM signals, the overlap between the optical and acoustic fields for intermodal SBS (pump at LP_{01} mode) are better compared to the intra-modal SBS.
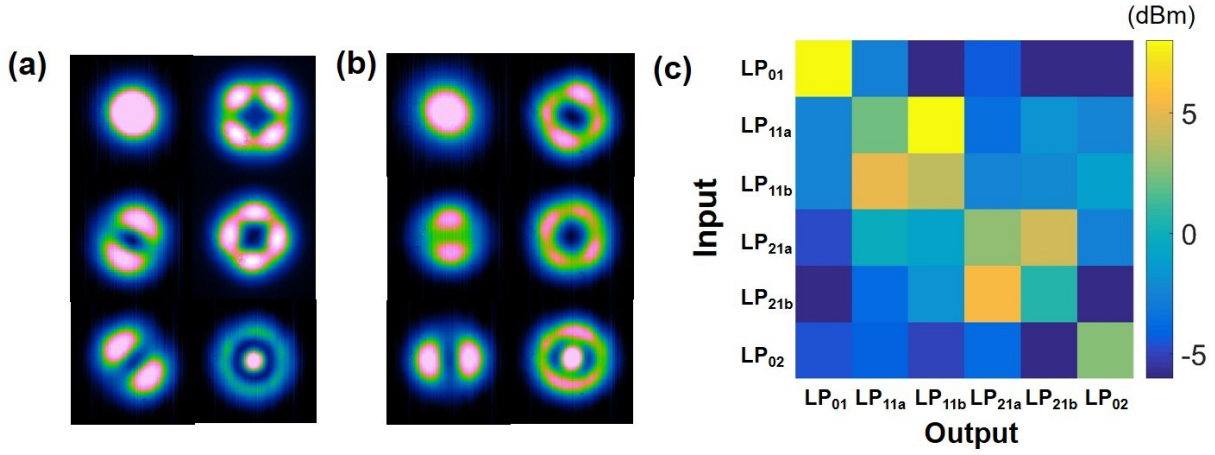
Figure 5-2: Output mode intensity profiles of (a) MSPL1 and (b) MSPL2 measured at 1550 nm, (c) mode transfer matrix of the pair of MSPLs with 1 km of FMF.

We used a pair of 6-to-1 MSPLs to realize the LP mode conversion between the SMF and the FMF. The tapered waist of the MSPL is essentially an FMF with a core and cladding diameter of 20 μm and 110 μm, respectively. The output facet of the MSPL can be easily spliced with a 4-LP mode FMF. We fabricated two 6-mode MSPLs, denoted MSPL1 and MSPL2, and measured their output mode profiles using a laser with a wavelength of 1550 nm. Figure 5-2(a) and 5-2(b) show the output mode profiles of MSPL1 and MSPL2, respectively. The six lowest-order LP modes were clearly observed with a mode conversion efficiency of ~70%. We also measured the mode transfer matrix from MSPL1 to MSPL2 with 1 km of FMF between them, the result is shown in Fig. 5-2(c). The mode selectivity between different mode groups was around 7 dB. But the

selectivity within the same mode group was much lower due to the orientation of the degenerate modes rotating within the circular core of the FMF. The total link loss for the LP_{01}, LP_{11}, LP_{21} and LP_{02} modes were measured to be 3.2 dB, 4.3 dB, 6.7 dB and 9.5 dB, respectively.

5.3 Experimental Setup
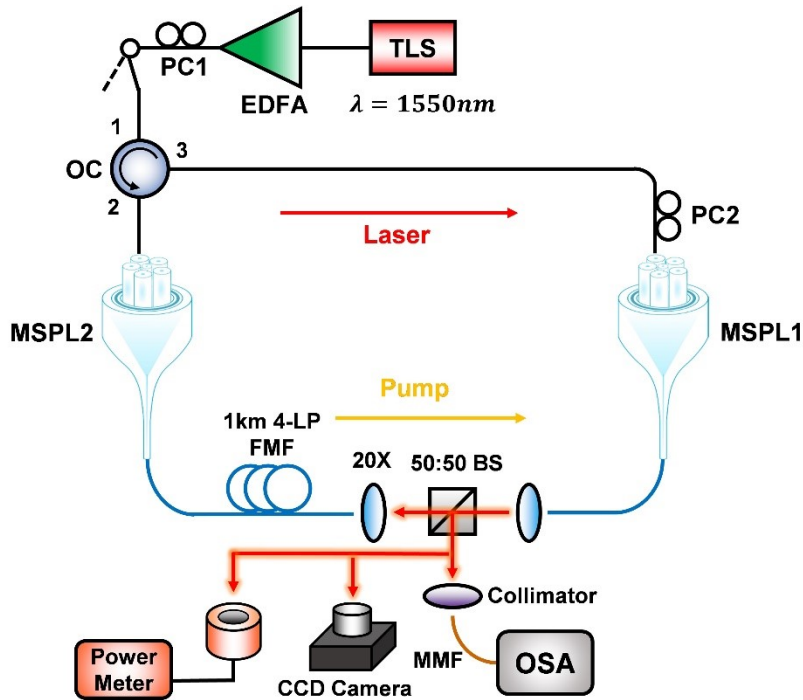
Figure 5-3: Experimental setup for the mode-selective few-mode BFLs.

The experimental setup for the transverse mode-selective BFLs is shown in Fig. 5-3. The pump was a tunable laser source (TLS) with a wavelength of 1550 nm, amplified by a commercial EDFA. For the intra-modal Brillouin lasing, the pump traveled through the circulator and was launched into MSPL2 to create the desired LP mode. The output of MSPL2 was spliced to 1 km of 4-LP mode FMF. The back scattered Stokes wave of the same mode went through the circulator from port 2 to port 3, and was injected into MSPL1 with the port mapping to the same LP mode.

41

The HOM signal from MSPL1 was collimated and coupled back into the 1km FMF with a pair of 20X objective lenses, and circulated clockwise as shown by the red arrow. The fiber coupling losses were less than 1 dB for all LP modes, and each objective lens introduced an additional 1 dB loss.

For the intermodal Brillouin lasing, the pump was directly launched into the LP_{01} port of MSPL2. The ports corresponding to the desired HOM for both MSPLs were connected to port 2 and 3 of the circulator. Due to intermodal SBS effects, all LP modes were scattered backwards even with only the fundamental mode as the pump. However, only the selected HOM can pass through the MSPL and oscillate inside the ring cavity. The laser came out from a 3-dB beam splitter (BS). The laser power and mode profiles were measured by a power meter and a CCD camera. We also coupled the laser into a piece of multimode fiber, after which its optical spectra were observed using an optical spectrum analyzer (OSA). Two SMF polarization controller (PC) were used to optimize the polarization states of the pump and Stokes waves, in order to maximize the Brillouin gain.

5.4 Results and Discussions

We measured the laser power of the LP_{01} mode, LP_{11} and LP_{21} modes based on both intra- and inter-modal SBS, as shown in Fig. 5-4(a). The results indicate that for all cases, lasing started after the pump power exceeded their threshold values. Over 24 mW of laser power were observed for all the LP modes. The LP_{01} lasing mode had the highest laser power and lowest threshold pump value. Its threshold pump power was only 40 mW, and the slope efficiency was 11.6%. The low slope efficiency was partly due to polarization state misalignment between the pump and Stokes

wave. Another reason was the relatively large insertion losses of the MSPLs. The slope efficiencies for LP$_{11}$ SBS lasing modes based on intra- and inter-modal SBS were 10.9% and 8.9%, respectively. The values for LP21 lasing modes based on intra- and inter-modal SBS were 10.5% and 8.6%, respectively. The lower laser power of the HOMs was mainly caused by a larger insertion loss of the photonic lantern pair compared to the LP$_{01}$ mode, and also the smaller overlap integral between the optical and guided acoustic fields. From Fig. 5-4(a), the laser power of HOMs based on intermodal SBS was always smaller than that based on intra-modal SBS, although their Brillouin gain coefficient are larger according to Table 5-1. This was because the strong backward SBS of the fundamental mode consumed part of the pump power. The polarization misalignment was another reason.
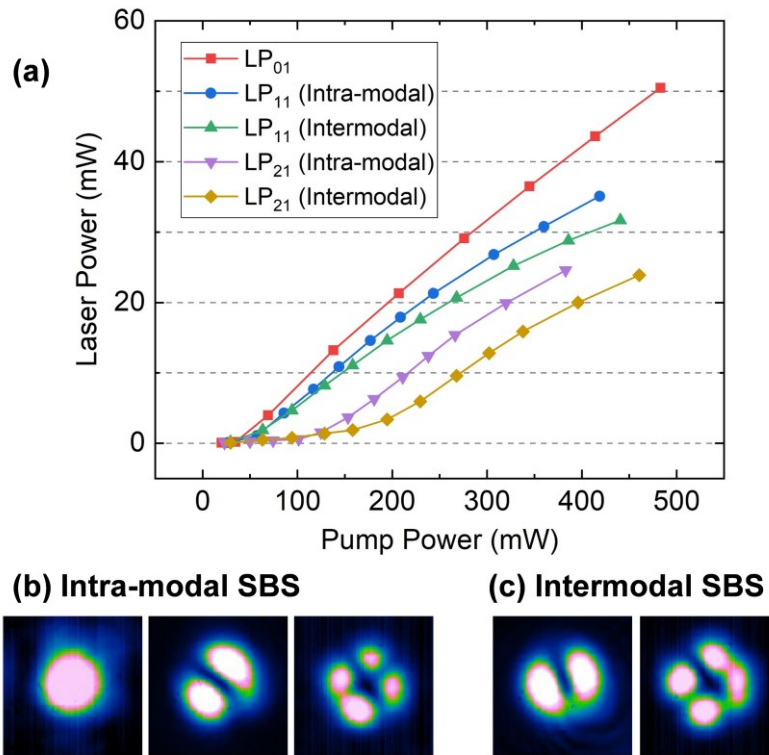
Figure 5-4: (a) Laser power vs. pump power for each LP lasing mode based on intra- and inter-modal SBS, mode intensity profiles of the few-mode BFLs based on (b) intra-modal SBS and (c) intermodal SBS.

43

The measured mode intensity profiles of BFLs of different LP modes based on intra-modal SBS and intermodal SBS configuration are shown in Fig. 5-4(b) and 5-4(c), respectively. We can see that their mode patterns are nearly ideal, the mode purities were over 90% for all cases thanks to the high mode selectivity of the MSPLs.
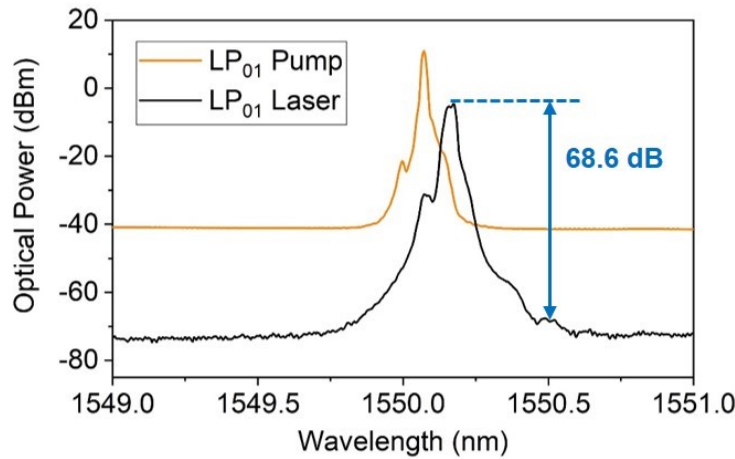
Figure 5-5: Optical spectra of the LP_{01} SBS lasing modes.

We measured the optical spectra of all the SBS lasing modes using an OSA (Ando AQ-6315e). The resolution of the OSA was set to be 0.02 nm. The optical spectra of the LP_{01} mode BFL together with its pump are shown in Fig. 5-5. The frequency downshift between the pump and the laser was around 0.1 nm, corresponding to a Brillouin frequency down shift of 10.6 GHz. There is a small peak in the laser spectra came from the reflection of the residual pump at the end of the FMF. It can be suppressed by angle cleaving the FMF ends. The OSNR was measured to be 68.6 dB, which is nearly 20 dB higher than that of the pump.
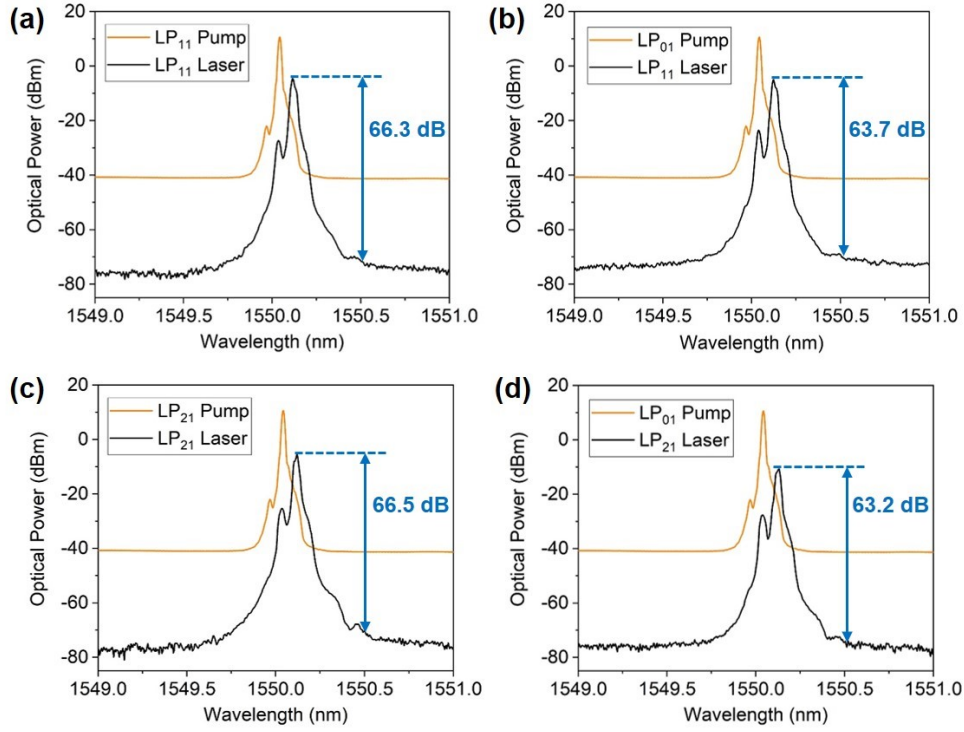
Figure 5-6: Optical spectra of LP_{11} modes based on (a) intra- and (b) inter-modal SBS, LP_{21} modes based on (c) intra- and (d) inter-modal SBS.

Figure 5-6(a) and 5-6(b) indicate the results for LP_{11} lasing modes based on intra- and inter-modal SBS, respectively. The shapes of their optical spectra looks similar, and the OSNRs were measured to be 66.3 dB and 63.7 dB. The results of LP_{21} lasing modes based on intra- and inter-modal SBS are shown in Fig. 5-6(c) and 5-6(d), respectively, their OSNRs were measured to be 66.5 dB and 63.2 dB.
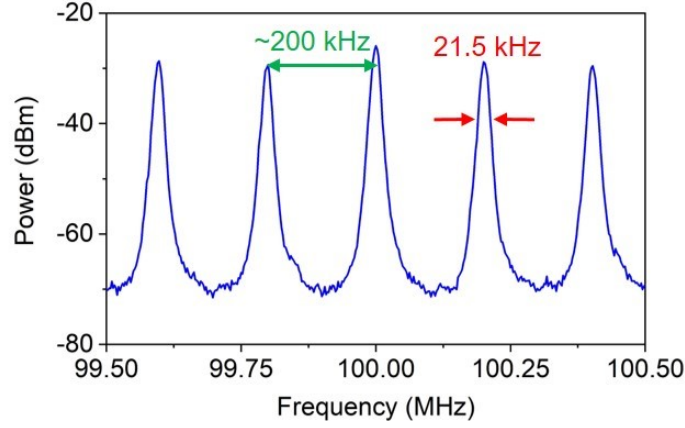
Figure 5-7: Beat-note spectrum of self-heterodyne linewidth measurement for the LP_{01} laser mode.

We also investigated the linewidth performance of each generated few-mode BFLs using self-heterodyne measurements, its working principle was described in [87]. We employed a 90:10 fiber coupler to let a small part of the laser get out at the SMF side before it went through MSPL1. The laser was then separated into two arms using a 3-dB coupler. One arm travelled through 25-km of SMF for the decorrelation, and the other arm was shifted by 100 MHz using an acousto-optic modulator. The beat-note spectrum was recorded using an electrical spectrum analyzer (hp ESA-L1500A), the resolution of the ESA was fixed to be 1 kHz. Figure 5-7 shows the beat-note spectrum for the LP_{01} mode BFL. There are multiple longitudinal modes observed with a spacing of around 200 kHz, which agrees well with the theoretical value. The 10-dB linewidth of the beat-note signal was 21.5 kHz, after fitting with the Lorentzian shape, corresponding to a 3-dB laser linewidth which was 3.6 kHz. The laser linewidth was narrowed by nearly two orders of magnitude compared to the pump which is ~200 kHz.

46
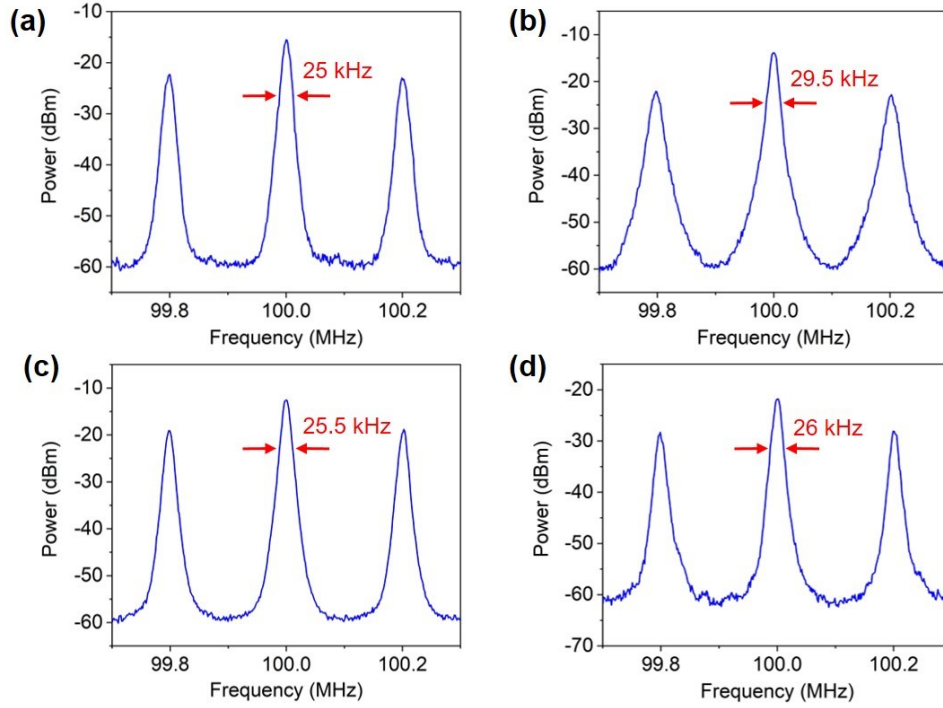
Figure 5-8: Beat-note electric spectrum for LP_{11} mode based on (a) intra- and (b) inter-modal SBS, LP_{21} mode based on (c) intra- and (d) inter-modal SBS.

The measured beat-note spectrum of LP_{11} lasing modes based on intra- and inter-modal SBS are shown in Fig. 5-8(a) and 5-8(b), their 3-dB linewidth were 4.17 kHz and 4.9 kHz, respectively. The results of LP_{21} mode BFLs are shown in Fig. 5-8(c) and 5-8(d), their 3-dB linewidth were 4.25 kHz and 4.33 kHz, correspondingly. It should be noticed that the intrinsic linewidths for all the LP modes were calculated to be less than 100 Hz. Linewidth broadening was mainly caused by the inhomogeneous broadening and instability of the environment, such as temperature fluctuations and mechanical perturbations, which can be improved by better isolating the fiber loop from the environment.

CHAPTER 6   SIMULTANEOUS GENERATION OF PHOTON AND PHONON LASERS

6.1 Introduction

Highly coherent acoustic waves have become an attractive resource that is beneficial for a number of applications. They are widely used for the study of laser radiation cooling, where the mechanical vibration is red-detuned by optical scattering forces [88-90]. They also paved the way for new strategies in precision metrology [91]. Based on the mechanical oscillation of a microsphere trapped in vacuum, short-range force detection with yoctonewton sensitivity has been achieved [92]. For gravitational wave detection, a mechanical wave can be used to decrease the quantum-mechanical noise based on the optical spring effect [93, 94]. Acoustic waves can also be used in optoelectronics for optical signal modulation.

A phonon laser, also called a saser, is the mechanical analogue of an optical laser, in which acoustic radiation (a sound wave) can be generated via sound amplification based on the stimulated emission of phonons. Sound (a mechanical vibration) can be described by phonons just as light can be considered to be made up of photons. This type of device is capable of producing coherent sound oscillations with characteristics that are similar to those of optical lasers, such as threshold, linewidth narrowing, and gain saturation. The concept of the phonon laser was first proposed in [95]. In the past decade, several impressive experiments have been reported. The first phonon laser experiment was conducted by Dr. Kent's group. In this experiment, a coherent oscillation of the phonon mode with a frequency of 441 GHz was generated when a bias voltage was applied to a semiconductor superlative [96].

Optomechanics is a powerful tool that creates the coupling between optical and mechanical waves [97]. In essence, it makes it possible to control acoustic phonons using light. For example, laser pumping an Mg^+ ion causes the stimulated emission of center-of-mass phonons, producing saturable amplification of motion [98]. Recently, an optical tweezer phonon laser was demonstrated that, based on the oscillation of a silica nanosphere, levitated in an optical tweezer under vacuum [99]. SBS is known to be a strong nonlinear effect that can be described as an interaction between light and sound waves. A compound microcavity system was proposed that operates similarly to a two-level laser system; it is based on the Brillouin scattering between two supermodes in a coupled microtoriods [100]. Phonon laser action at a frequency of 23 MHz has been observed. In addition, another work reported the experimental excitation of whispering-gallery typed mechanical resonances ranging from 49 to 1400 MHz via forward SBS between high-order transverse optical modes in a silica microsphere resonator [101]. A phonon laser with Hermite-Gaussian like acoustic modes was also generated in a TeO_2 crystal at cryogenic temperatures [102].

In this work, we propose a system that, for the first time to the best of our knowledge, can generate both phonon and photon lasers simultaneously in a fiber ring cavity. The low-frequency acoustic flexural wave is generated via a forward SBS between the fundamental and high-order transverse optical modes in the two-mode FMF. Using the LP_{01} mode as the pump, both the generated Stokes wave in LP_{11} mode and a flexural acoustic wave can resonate inside the same ring cavity. The coherent oscillation of the optical wave enhances the gain of the acoustic phonons and vice versa. We also demonstrate this system experimentally using a 10-meter-long reduced cladding FMF. Both the optical laser power and phonon laser linewidth were characterized.

6.2 Theory and Simulation Results

The SBS effects in the optical fiber can be classified into backward and forward SBS. For both processes, energy and momentum are conserved:

$$\omega_p = \omega_s + \Omega_a \qquad (6\text{-}1)$$

$$k_p = k_s + k_a , \qquad (6\text{-}2)$$

where ω_p and ω_s are the frequencies of the pump and Stokes waves, respectively; Ω_a is the emitted acoustic phonon frequency; k_p and k_s are the propagation constants of the pump and Stokes waves, respectively; and k_a is the wave vector of the acoustic phonon. Fig. 6-1 shows the comparison in terms of the conservation of energy and momentum between backward and forward SBS. The blue and red lines are the dispersion curves of the optical modes, and the green lines are the dispersion curves of the acoustic modes. For the backward SBS shown in Fig. 6-1(a), the scattered Stokes wave propagates in a backward direction, while the acoustic wave propagates in a forward direction. In this case, the generated acoustic modes are mainly longitudinal modes that are confined inside the fiber core area. The acoustic frequency is on the order of 10 GHz. In silica, acoustic waves at such high frequencies are highly damped and unable to create acoustic feedback. In strong contrast, for the forward SBS shown in Fig. 6-1(b), both the Stokes and acoustic waves propagate in the forward direction. The acoustic flexural modes are generated via the intermodal SBS between two different transverse optical modes. In this case, the generated phonon frequencies can drop to the MHz level. This low-frequency phonon propagation in silica fiber cladding has a relatively long lifetime, which makes it possible to generate a phonon laser.
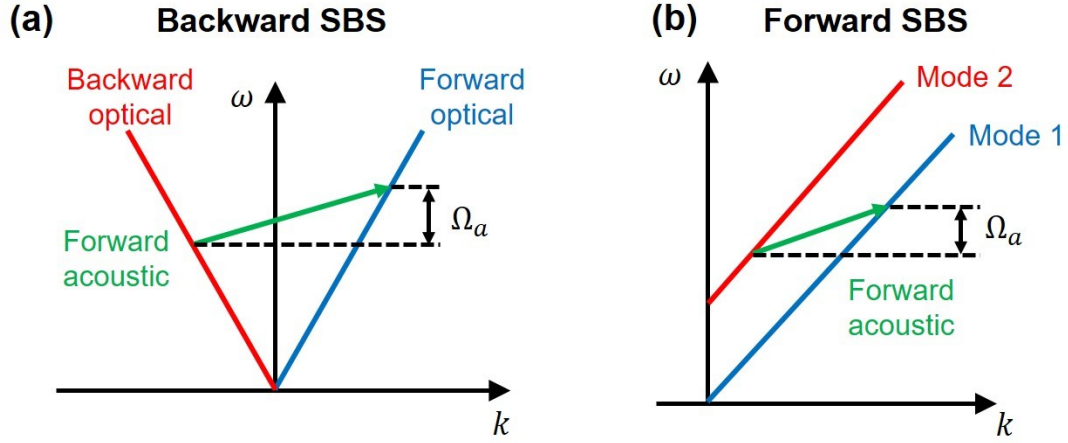
Figure 6-1: Dispersion diagrams under energy and momentum conservation conditions for (a) backward SBS and (b) forward SBS.

The fiber we used for our proposed system was a reduced cladding two-mode FMF (TMF) made of silica with GeO_2-doped core. The core and cladding diameters were 6.8 um and 60 um, respectively. We choose 980 nm as the operation wavelength because it is easier to obtain a fiber coupled high-power pump diode at this wavelength. The measured fiber refractive index profile is shown in Fig. 6-2(a). It has a step-index-shaped profile with an NA of 0.13, which corresponds to fiber number V=2.83, ensuring that it supports two LP modes at the operation wavelength. We simulated the optical modes of this fiber at 980 nm, and their electric field distributions are shown in Fig. 6-2(b). We can see that both the LP_{01} and LP_{11} (even and odd) modes were guided in the core region. The propagation constant difference between the two modes was $\Delta k = 1.9417 \times 10^{-4}$.
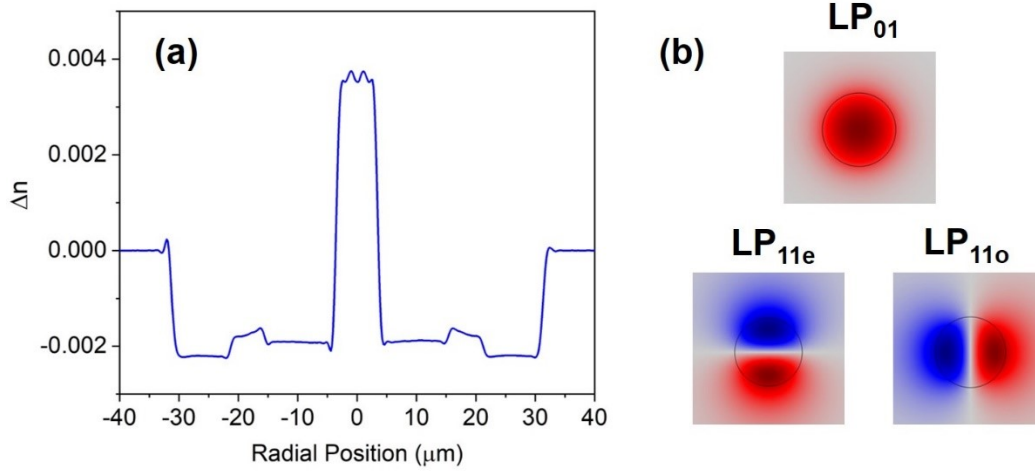
Figure 6-2: (a) Measured refractive index profile of the reduced cladding FMF, (b) simulated electric fields of the guided optical modes at a wavelength of 980 nm.

The flexural acoustic modes mediate the forward intermodal SBS. Unlike the optical modes that are guided in the core, the fields of flexural acoustic waves are distributed in the entire cladding area. The general solutions for the displacement field distributions in a silica cylinder can be expressed as [103]:

$$u_r(r, \varphi, z) = U(r) \begin{Bmatrix} \sin(n\varphi) \\ \cos(n\varphi) \end{Bmatrix} e^{i(\Omega t - k_a z)} \tag{6-3a}$$

$$u_\varphi(r, \varphi, z) = V(r) \begin{Bmatrix} \cos(n\varphi) \\ -\sin(n\varphi) \end{Bmatrix} e^{i(\Omega t - k_a z)} \tag{6-3b}$$

$$u_z(r, \varphi, z) = W(r) \begin{Bmatrix} \sin(n\varphi) \\ \cos(n\varphi) \end{Bmatrix} e^{i(\Omega t - k_a z)}, \tag{6-3c}$$

where n is an integer describing the azimuthal order of the flexural mode. For the modes generated by the SBS between the LP_{01} and LP_{11} modes, n always equals 1. The radial variation is given by:

$$U(r) = A k_l J_n'(k_l r) + B k_a J_n'(k_t r) + C \frac{n}{r} J_n(k_t r) \tag{6-4a}$$

$$V(r) = A \frac{n}{r} J_n(k_l r) + B \frac{k_a n}{k_t r} J_n(k_t r) + C k_t J_n'(k_t r) \tag{6-4b}$$

52

$$W(r) = -i[Ak_a J_n(k_l r) - Bk_t J_n(k_t r)], \tag{6-4c}$$

where the parameters k_l and k_t are given by:

$$k_l^2 = \frac{\Omega^2}{c_l^2} - k_a^2 \tag{6-5a}$$

$$k_t^2 = \frac{\Omega^2}{c_t^2} - k_a^2, \tag{6-5b}$$

where c_l and c_t are the longitudinal and transverse acoustic velocities of bulk silica, respectively. According to the traction-free boundary condition, the three components of the stress tensor $T_{rr}, T_{rz}, T_{r\phi}$ must equal zero at the boundary between silica and air, making it possible to find the dispersion relation and constants A, B, and C for each flexural mode. For our system, we used the lowest-order flexural mode with n=1 to build the phonon laser due to this mode having the lowest dissipation rate and no cut-off condition.

Next, we calculated the lowest-order flexural acoustic mode taking part in the intermodal forward SBS in our reduced cladding FMF. Based on its dispersion relation, the frequency of the phonon mode that satisfied the momentum conservation was 5.11 MHz, which corresponds to a phase velocity of $v_F = 1654 \, m/s$. The damping rate of the ultrasonic wave is proportional to the square of the phonon frequency in pure silica [104]. For the acoustic wave at such a low frequency, the damping rate is $\Gamma_B = 35.4 \, Hz$, and the resulting phonon loss is $\alpha_F = \Gamma_B/v_F = 0.022/m$. We calculated the displacement field distributions in the radial direction for this acoustic mode, and the results are shown in Fig. 6-3. The field is distributed throughout the entire cladding area, and the particle displacements are mainly in the transversal direction.
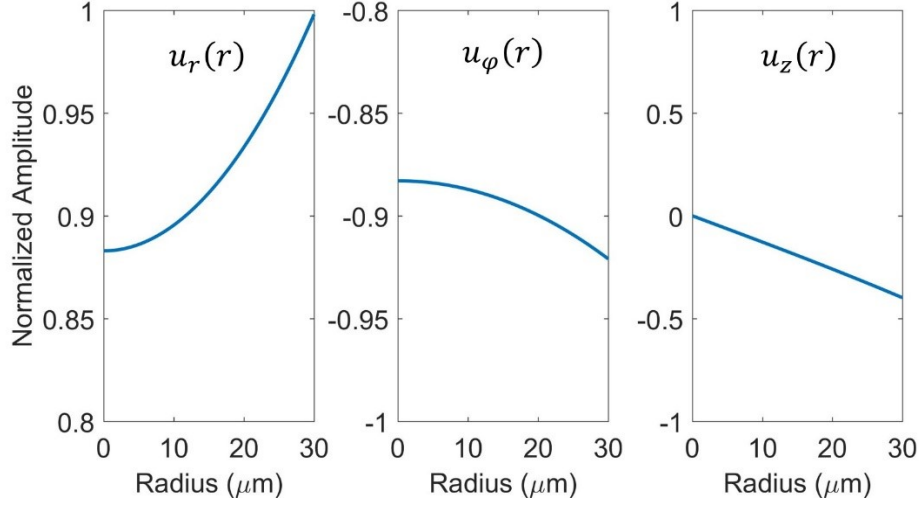
Figure 6-3: Displacement field distributions in the radial direction for the lowest-order flexural mode with n=1 at a frequency of 5.11 MHz.

The interactions between acoustic and optical waves are described by the three-wave coupled-wave equations. We define the normalized amplitude as $|a_m| = \sqrt{P_m/P_{tot}}$. Here, m could be p, s, or F to represent the pump, Stoke wave, and flexural acoustic wave, respectively. P_{tot} is the total incident power. The coupled amplitude equations can be expressed as follows [105]:

$$\frac{\partial a_p}{\partial z} + \frac{\alpha}{2} a_p = -j\kappa_p a_F a_s \tag{6-6a}$$

$$\frac{\partial a_s}{\partial z} + \frac{\alpha}{2} a_s = -j\kappa_s a_F^* a_p \tag{6-6b}$$

$$\frac{\partial a_F}{\partial z} + \frac{\alpha_F}{2} a_F = -j\kappa_F a_p a_s^* , \tag{6-6c}$$

where α is the attenuation of the optical wave at 980 nm, which is nearly 0.001/m. The coupling coefficients are defined by:

$$\kappa_m = \omega_m/C_F, \text{ m=p, s, F} \tag{6-7}$$

The parameter C_F is given by:

$$C_F = \frac{n_p n_s}{Q(\partial \varepsilon_r / \partial s)} \sqrt{\frac{2\pi v_{gp} v_{gs} v_{gF} E a^2}{P_{tot}}}, \tag{6-8}$$

where n_p and n_s are the effective indexes of the pump and Stokes modes, respectively; v_{gp} and v_{gs} are the group velocities of the pump and Stokes waves, respectively; and v_{gF} is the group velocity of the flexural acoustic mode, which is defined as:

$$v_{gF} = v_F / (1 - \frac{\omega_F}{v_F} \frac{\partial v_F}{\partial \omega_F}) \tag{6-9}$$

In Eq. (6-8), $\partial \varepsilon_r / \partial s$ is the electrostriction parameter. For fused silica, its value is 3.3. E is Young's modulus, which equals $73 GN/m^2$ for pure silica, and a is the fiber cladding radius. The overlap integral Q is given by:

$$Q = \frac{1}{a} \iint e_{01}(r, \varphi) e_{11}(r, \varphi) r^2 cos\varphi dr d\varphi, \tag{6-10}$$

where $e_{01}(r, \varphi)$ and $e_{11}(r, \varphi)$ are the normalized transverse electric field distributions for the LP$_{01}$ and LP$_{11}$ optical modes, respectively.

Next, we calculated the small signal gains for both the LP$_{11}$ mode Stokes wave and the flexural acoustic wave in 10 meters of uncoated FMF. The incident pump power was fixed as 400 mW, and its 3-dB linewidth was 1 MHz. The initial LP$_{11}$ mode power at the beginning of the fiber caused by the spontaneous scattering from the pump can be estimated by [106]:

$$P_s(z = 0) = \frac{v_s \Delta v_p kT}{f_F}, \tag{6-11}$$

where k is Boltzmann's constant, and Δv_p is the pump linewidth. The spontaneous scattered optical power is $7.57 \times 10^{-8} W$, which is accompanied by an initial acoustic power of $3.45 \times 10^{-14} W$. These weak signals can be considered to be the seeds that trigger the photon and

phonon lasing. We solved the three wave coupled-wave equations numerically using a step size of 1mm, and the results are shown in Fig. 6-4.
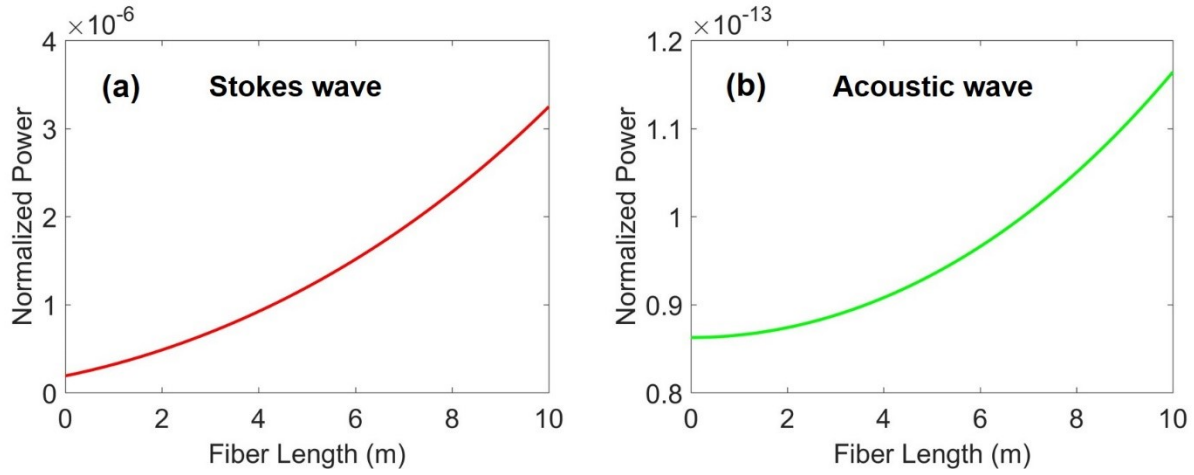
Figure 6-4: Calculated small signal gain for the (a) LP_{11} mode Stokes wave and (b) flexural acoustic wave in 10 meters of FMF with a pump power of 400mW.

As can be seen from Fig. 6-4, the power of both the LP_{11} optical wave and flexural acoustic wave keep increasing within the 10-meter-long TMF. The total gain for the Stokes wave is 12.3 dB. The gain of the phonon wave is smaller due to its lower coupling efficient and higher loss. In the 10-meter FMF, the phonon power is increased by a factor of 1.35. These results indicate that it is possible to produce both photon and phonon mode lasing in the same fiber laser cavity with a proper design.
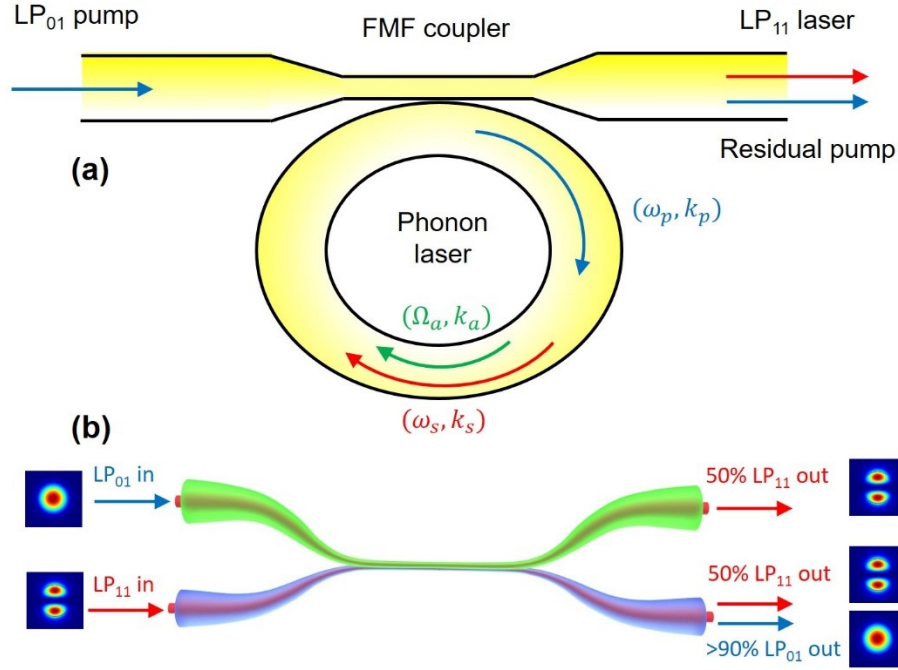
Figure 6-5: (a) Schematic setup for a TMF-based system that can simultaneously generate photon and phonon lasers, (b) schematic and functions of the FMF coupler.

The schematic setup of the proposed phonon and photon laser system is shown in Fig. 6-5(a). It contains a TMF ring cavity. The optical pump in LP_{01} mode from the incident FMF was coupled into the ring cavity through an FMF coupler. The structure of the fiber coupler is shown in Fig. 6-5(b). It is a fused-fiber-type coupler for two fibers having the same core size but different cladding sizes. The outer diameter for the other fiber is 80 μm. This design can break the degeneracy of the acoustic modes so that the first fiber will not couple to the other fiber even if the two fibers are melted at their taper waist. Since the two LP modes have different coupling coefficients, we can control their power split ratio by adjusting the length of the waist. For the LP_{01} mode, the power is nearly completely coupled into the other fiber. For the LP_{11} mode, the coupler performs as a 50:50 splitter. It should be noted that the transition lengths of both sides need to be long enough (>2.5 cm) so that the acoustic wave can propagate through the coupler without notable

power loss. The total length of the FMF ring cavity in our design is 10 meters. The intermodal forward SBS will occur inside the 10-meter TMF, and both the LP_{11} mode Stokes and flexural acoustic waves will be amplified. Once the phase matching conditions are satisfied for both photon and phonon modes, the power for both of them will keep increasing until the round trip gain equals the loss. Once the steady state is reached, the flexural acoustic wave will keep resonating inside the fiber ring cavity, while the LP_{11} optical mode will receive a constant output from the coupler. The free spectral range (FSR) of the LP_{11} optical mode is around 20 MHz, which is larger than the Brillouin gain bandwidth. In order to satisfy its phase matching condition, we need to gradually sweep the pump frequency to let the gain peak overlap with one of the longitudinal modes. The FSR of the acoustic mode is less than 200 Hz, so it could be easily find a frequency within the gain bandwidth that satisfies its phase matching condition.

Next, we simulated the power of the photon and phonon lasers. Having reached the steady state condition, the gain of the 10-meter FMF will balance the round trip loss for both lasers. For the LP_{11} mode optical laser, there is 3-dB loss coming from the 50:50 output coupler, plus another 3 dB insertion loss from the FMF coupler. For the phonon laser, the round trip loss mainly comes from the transition section of the FMF coupler, which is estimated to be 0.8 dB on each side. There is also another 0.1 dB propagation loss from the fiber coupler because when the fiber cladding size changed, the conservation of momentum was no longer satisfied, meaning that there is no gain in this region. The steady state conditions can be expressed by:

$$P_s(z = L) = 4 \times P_s(z = 0) \tag{6-12}$$

$$P_F(z = L) = 1.5 \times P_F(z = 0) \tag{6-13}$$

We iteratively solved the three-wave coupled-wave equations by gradually increasing the initial power of both the photon and phonon waves until the steady state conditions were satisfied for both of them. We define the power right after the FMF coupler at $z = 0$ to be the intra-cavity laser power. We plot the laser power at different pump powers in Fig. 6-6.
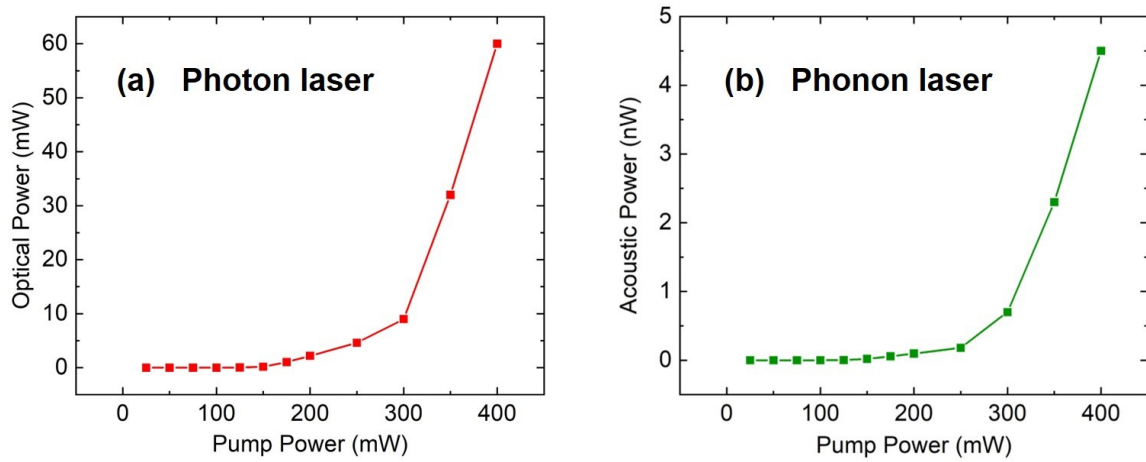
Figure 6-6: Simulated laser power vs. pump power for (a) LP_{11} mode photon laser and (b) phonon laser.

Fig. 6-6(a) shows the laser power of the LP_{11} mode photon laser at different pump powers, and Fig. 6-6(b) shows the power of the flexural mode phonon laser. We find that the photon lasing starts prior to the phonon lasing because it is easier for an optical wave to accumulate enough gain for the lasing. The threshold pump power of the photon laser is 150 mW, which is lower than that of the phonon laser (300 mW). At pump powers below the phonon laser threshold, the LP_{11} mode optical laser power is much lower. Once the pump power exceeds the phonon laser threshold, the power of both lasers increases linearly in a dramatic fashion due to the higher acoustic power enhancing the gain for the Stokes wave and vice versa. At an incident pump power of 400 mW, the intra-cavity photon laser power was calculated to be over 60 mW, whereas the phonon laser had a power of 4.5 nW. For a Brillouin fiber laser with such a low acoustic dissipation rate, the

resulting optical laser would be exceptional coherent with the pump, which means they would have similar linewidths. The linewidth of the phonon laser is much narrower and is supposed to be only tens of Hertz.

6.3 Experimental Setup and Results
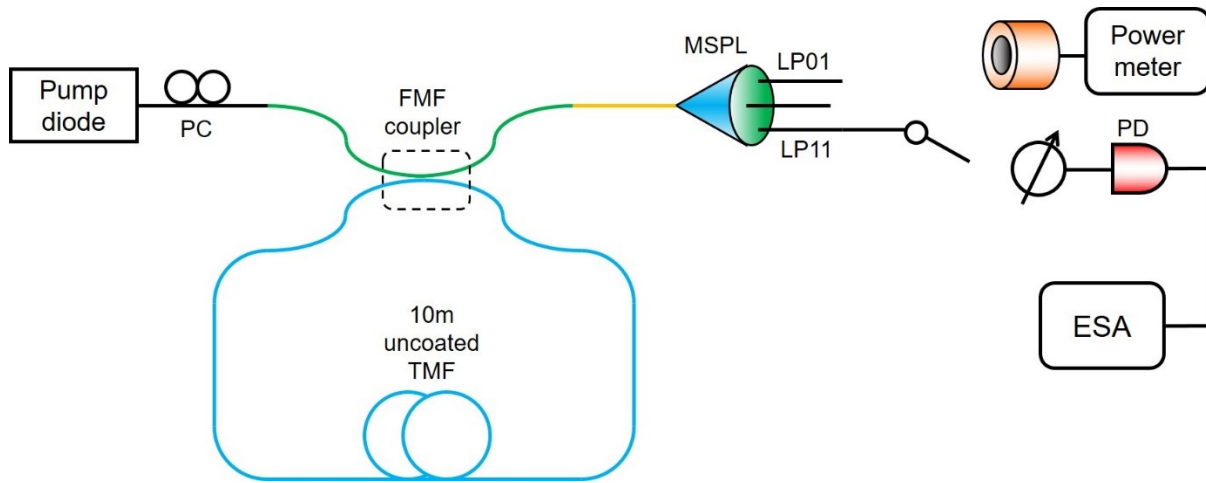
Figure 6-7: Experimental setup for the simultaneous generation of the photon and phonon lasers in a TMF ring cavity.

The experimental setup of our photon and phonon laser system is shown in Fig. 6-7. The 976 nm fiber-coupled pump diode has a linewidth of ~1 MHz and a maximum output power of 400 mW. Its TEC controller can control the operation temperature precisely with a step size of 0.001 °C. The fundamental mode pump was launched into the TMF with an 80 μm outer diameter and completely coupled into the TMF with a 60 μm outer diameter. A PC was used to optimized the pump power that coupled into the fiber ring cavity. The forward intermodal SBS took place in the 10-meter uncoated TMF, and both the LP_{11} mode Stokes and flexural acoustic waves were amplified and travelling clockwise. We gradually swept the pump frequency via the operating

temperature. Once the photon and phonon lasing condition was satisfied, the phonon laser was oscillating inside the 10-meter TMF ring cavity, while the LP_{11} mode photon laser was partially coupled out through the FMF coupler, together with the LP_{01} mode residual pump. There is a frequency downshift between the photon laser and the pump of around 5.1MHz, which is equal to the phonon laser frequency. We employed a low-crosstalk 3-mode MSPL to separate the pump and the Stokes waves of different LP modes. We measured the optical power of the LP_{11} mode Stokes wave with a power meter. We also characterized the beat-note electrical spectrum between the pump and the Stokes wave with an ESA.
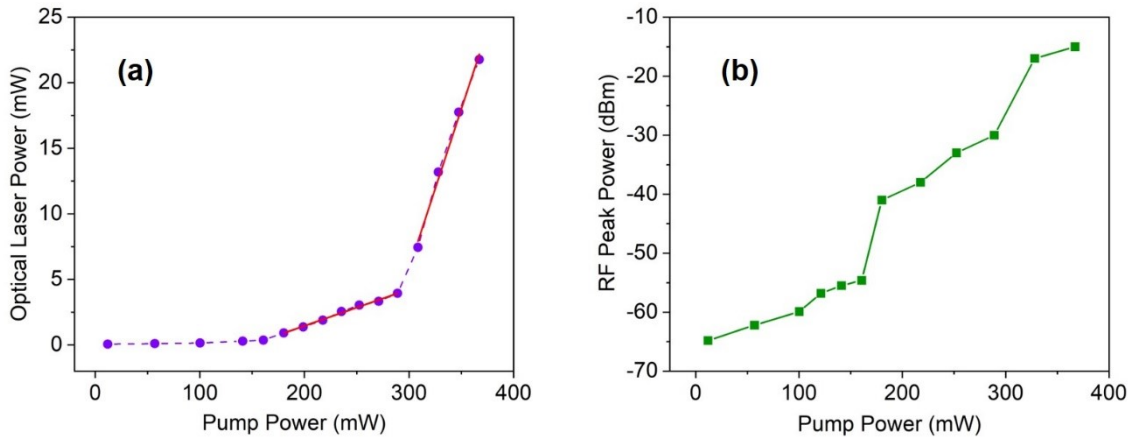
Figure 6-8: (a) Measured optical power of the LP_{11} mode Stokes wave, (b) RF peak power of the beat-note electrical spectra at each pump power.

The measured LP_{11} mode optical power at different pump powers is shown in Fig. 6-8(a). We can clearly see that there are two thresholds that correspond to the photon laser and phonon laser. The threshold pump power of the photon laser was 180 mW, and the Stokes wave starts lasing beyond that. However, due to lack of acoustic power, the output optical laser power was low at only a few milliwatts. When the pump power increased to 308 mW, the phonon laser began

operation. The stronger acoustic field also enhanced the gain of the Stokes wave. The output laser slope became much sharper in this region. The maximum optical laser power was measured as 21.8 mW at a pump power of 367 mW. We also checked the peak power on the RF beat-note spectra at different pump powers, as shown in Fig. 6-8(b). The resolution bandwidth for this measurement was fixed at 10 kHz. We can see that there are two obvious jumps in the RF peak power matching the thresholds of the photon and phonon lasers.
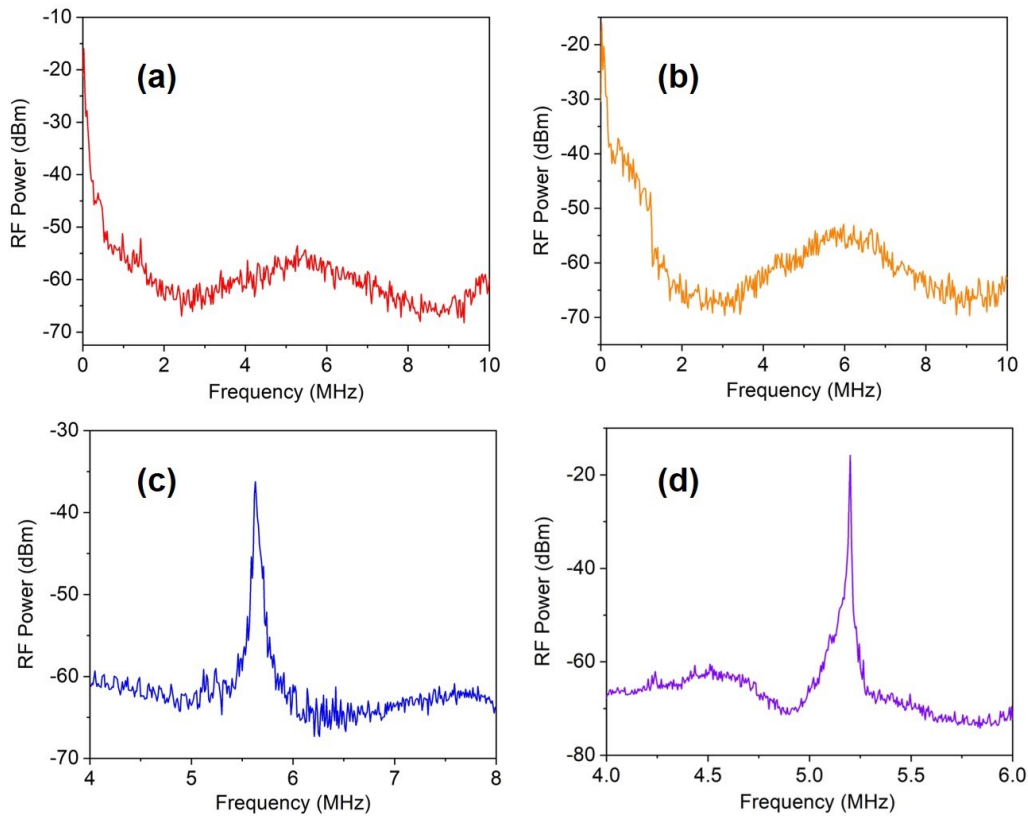
Figure 6-9: Beat-note electrical spectrum between pump and Stokes wave at pump powers of (a) 100mW, (b) 161mW, (c) 271mW, and (d) 367mW.

We recorded the beat-note electrical spectrum at different incident pump powers, as shown in Fig. 6-9. Their transitions in terms of electrical spectrum lineshape can be clearly observed. In the first state, only some spontaneous scattering signals are detected, as shown in Fig. 6-9(a). The

3-dB linewidth was 2.2 MHz at a central frequency of 5.4 MHz, which agrees with the broad gain bandwidth of spontaneous Brillouin scattering. In the second state, SBS became the dominant phenomenon, as shown in Fig. 6-9(b). This time, the 3-dB linewidth was narrowed down to 1.6 MHz as a result of the Brillouin gain. The beat-note spectrum of the photon laser is shown in Fig. 6-9(c). We can see that there is a much stronger peak at the f 5.6 MHz frequency. Its 3-dB linewidth was measured to be 30 kHz. For the forward-SBS-based laser system, since the acoustic damping is not as strong as the backward SBS, the pump linewidth narrowing effect is not as strong, which means that the Brillouin laser has a similar linewidth to that of the pump. Finally, we observed the results for the photon and phonon lasers, as shown in Fig. 6-9(d). The phonon laser has a 3-dB linewidth of only 1.7 kHz at a frequency of 5.2 MHz. The drift of the phonon center frequency was caused by the fluctuation of the pump frequency, and the frequency difference between the pump and optical longitudinal mode changed. For the phonon lasing case, the pump and the optical laser were exceptionally coherent. It should be noted that the intrinsic acoustic dissipation rate of the phonon at such a low frequency is only 50 Hz. The increase in the phonon laser's emission linewidth was mainly caused by the additional acoustic losses that came from the fiber and coupler.

CHAPTER 7 CONCLUSIONS

First of all, we proposed a low-crosstalk FM-EDFA by exploiting the unitary property of the coupling matrix of a symmetric PL. We also demonstrated a 3-mode FM-EDFA with a small-signal gain larger than 25 dB and crosstalk below -10 dB over the entire C-band experimentally. This type of FM-EDFA can replace multiple parallel single-mode EDFAs in SMF trunk lines and networks. Using our scheme, the overall costs of long-haul fiber optics transmission systems could be greatly reduced.

In the area of amplification of high-order spatial modes, we also demonstrated an EDFA for OAM modes using an annular-core PL. In the active FMF, both the first- and second-order OAM modes were amplified with small-signal gains of up to 22.1 dB and 16.7 dB, respectively. The amplified OAM mode intensity profiles were clearly observed, and our scheme works well for the entire C-band. Such high-power OAM modes could be used in microscopy systems to enhance the resolution of images by orders of magnitude for a variety of structures.

We also demonstrated an intra-cavity transverse mode-switchable Er-doped fiber laser using a 6-mode MSPL experimentally. The lasing mode can be switched between the six LP modes and two donut modes by simply switching the input port of the MSPL. The generated lasers' mode profiles look nearly ideal. These high-purity HOM lasers could be beneficial in a variety of applications ranging from fiber sensors and laser material processing to the detection of gravitational waves.

Additional techniques for the generation of HOM fiber lasers were explored in this thesis by utilizing SBS in the passive FMF. We presented a transverse mode-selective BFL based on an

intermodal SBS effect, where the fundamental mode was the pump. In this configuration, pump mode converters are not required, which can greatly reduce the costs and complexity of the entire laser system.

Finally, we proposed a fiber ring cavity that can simultaneously produce photon and phonon lasing based on forward intermodal SBS. We experimentally demonstrated for the first time, to the best of our knowledge, a two-domain ring laser using a 10-meter reduced-cladding TMF. The measured LP_{11} mode optical laser power was over 20 mW, and the phonon laser linewidth was on the order of 1 kHz. This is a brand-new, never-before-observed physical phenomenon. It could pave the way for future investigations of optomechanics and narrow-linewidth laser sources. It also has potential in applications such as acoustic and optical trapping and high-quality microwave signal generation.

LIST OF REFERENCES

1. S. Ramachandran, J. M. Fini, M. Mermelstein, J. W. Nicholson, S. Ghalmi, and M. F. Yan, "Ultra‑large effective‑area, higher‑order mode fibers: a new strategy for high‑power lasers," Laser & Photonics Reviews **2**, 429-448 (2008).

2. J. M. Fini and S. Ramachandran, "Natural bend-distortion immunity of higher-order-mode large-mode-area fibers," Optics letters **32**, 748-750 (2007).

3. D. Richardson, J. Fini, and L. E. Nelson, "Space-division multiplexing in optical fibres," Nature photonics **7**, 354-362 (2013).

4. N. Bai, E. Ip, Y.-K. Huang, E. Mateo, F. Yaman, M.-J. Li, S. Bickham, S. Ten, J. Liñares, and C. Montero, "Mode-division multiplexed transmission with inline few-mode fiber amplifier," Optics express **20**, 2668-2680 (2012).

5. R. Ryf, S. Randel, A. H. Gnauck, C. Bolle, A. Sierra, S. Mumtaz, M. Esmaeelpour, E. C. Burrows, R.-J. Essiambre, and P. J. Winzer, "Mode-Division Multiplexing Over 96 km of Few-Mode Fiber Using Coherent 6 x 6 MIMO Processing," Journal of Lightwave technology **30**, 521-531 (2011).

6. R. Ryf, M. Mestre, S. Randel, C. Schmidt, A. Gnauck, R.-J. Essiambre, P. Winzer, R. Delbue, P. Pupalaikis, and A. Sureka, "Mode-multiplexed transmission over a 209-km DGD-compensated hybrid few-mode fiber span," IEEE Photonics Technology Letters **24**, 1965-1968 (2012).

7. A. Van Newkirk, J. Antonio-Lopez, A. Velazquez-Benitez, J. Albert, R. Amezcua-Correa, and A. Schülzgen, "Bending sensor combining multicore fiber with a mode-selective photonic lantern," Optics Letters **40**, 5188-5191 (2015).

8. A. Li, Y. Wang, Q. Hu, and W. Shieh, "Few-mode fiber based optical sensors," Optics express **23**, 1139-1150 (2015).

9. Y. Weng, E. Ip, Z. Pan, and T. Wang, "Single-end simultaneous temperature and strain sensing techniques based on Brillouin optical time domain reflectometry in few-mode fibers," Optics express **23**, 9024-9039 (2015).

10. Y. Xu, M. Ren, Y. Lu, P. Lu, X. Bao, L. Wang, Y. Messaddeq, and S. LaRochelle, "Multi-parameter sensor based on stimulated Brillouin scattering in inverse-parabolic graded-index fiber," Optics letters **41**, 1138-1141 (2016).

11. J. Hamazaki, R. Morita, K. Chujo, Y. Kobayashi, S. Tanda, and T. Omatsu, "Optical-vortex laser ablation," Optics express **18**, 2144-2151 (2010).

12.　M. Meier, V. Romano, and T. Feurer, "Material processing with pulsed radially and azimuthally polarized laser radiation," Applied Physics A **86**, 329-334 (2007).

13.　N. Sanner, N. Huot, E. Audouard, C. Larat, and J.-P. Huignard, "Direct ultrafast laser micro-structuring of materials using programmable beam shaping," Optics and Lasers in Engineering **45**, 737-741 (2007).

14.　S. Chelkowski, S. Hild, and A. Freise, "Prospects of higher-order Laguerre-Gauss modes in future gravitational wave detectors," Physical Review D **79**, 122002 (2009).

15.　A. Noack, C. Bogan, and B. Willke, "Higher-order Laguerre–Gauss modes in (non-) planar four-mirror cavities for future gravitational wave detectors," Optics Letters **42**, 751-754 (2017).

16.　J. Daniel and W. Clarkson, "Rapid, electronically controllable transverse mode selection in a multimode fiber laser," Optics express **21**, 29442-29448 (2013).

17.　B. Sun, A. Wang, L. Xu, C. Gu, Y. Zhou, Z. Lin, H. Ming, and Q. Zhan, "Transverse mode switchable fiber laser through wavelength tuning," Optics letters **38**, 667-669 (2013).

18.　L. Li, M. Wang, T. Liu, J. Leng, P. Zhou, and J. Chen, "High-power, cladding-pumped all-fiber laser with selective transverse mode generation property," Applied Optics **56**, 4967-4970 (2017).

19.　D. Lin and W. Clarkson, "Polarization-dependent transverse mode selection in an Yb-doped fiber laser," Optics letters **40**, 498-501 (2015).

20.　W. Lubeigt, G. Valentine, J. Girkin, E. Bente, and D. Burns, "Active transverse mode control and optimisation of an all-solid-state laser using an intracavity adaptive-optic mirror," Optics Express **10**, 550-555 (2002).

21.　S. Ngcobo, I. Litvin, L. Burger, and A. Forbes, "A digital laser for on-demand laser modes," Nature communications **4**, 1-6 (2013).

22.　C. Tian, S. Yu, S. Cai, M. Lan, and W. Gu, "Fiber laser for on-demand mode generation in 1550 nm band," Photonics Research **5**, 256-260 (2017).

23.　S. Wang, S.-l. Zhang, P. Li, M.-h. Hao, H.-m. Yang, J. Xie, G.-y. Feng, and S.-h. Zhou, "Generation of wavelength-and OAM-tunable vortex beam at low threshold," Optics Express **26**, 18164-18170 (2018).

24.　D. Lin, J. Daniel, and W. Clarkson, "Controlling the handedness of directly excited Laguerre–Gaussian modes in a solid-state laser," Optics letters **39**, 3903-3906 (2014).

25.　D. Kim and J. Kim, "Direct generation of an optical vortex beam in a single-frequency Nd: YVO 4 laser," Optics letters **40**, 399-402 (2015).

26. R. Zhou, J. W. Haus, P. E. Powers, and Q. Zhan, "Vectorial fiber laser using intracavity axial birefringence," Optics Express **18**, 10839-10847 (2010).

27. D. Naidoo, F. S. Roux, A. Dudley, I. Litvin, B. Piccirillo, L. Marrucci, and A. Forbes, "Controlled generation of higher-order Poincaré sphere beams from a laser," Nature Photonics **10**, 327-332 (2016).

28. I. A. Litvin, S. Ngcobo, D. Naidoo, K. Ait-Ameur, and A. Forbes, "Doughnut laser beam as an incoherent superposition of two petal beams," Optics letters **39**, 704-707 (2014).

29. T. Wang, F. Shi, Y. Huang, J. Wen, Z. Luo, F. Pang, T. Wang, and X. Zeng, "High-order mode direct oscillation of few-mode fiber laser for high-quality cylindrical vector beams," Optics express **26**, 11850-11858 (2018).

30. Y. Huang, F. Shi, T. Wang, X. Liu, X. Zeng, F. Pang, T. Wang, and P. Zhou, "High-order mode Yb-doped fiber lasers based on mode-selective couplers," Optics express **26**, 19171-19181 (2018).

31. R. Chen, J. Wang, X. Zhang, A. Wang, H. Ming, F. Li, D. Chung, and Q. Zhan, "High efficiency all-fiber cylindrical vector beam laser using a long-period fiber grating," Optics letters **43**, 755-758 (2018).

32. J. Li, J. Du, L. Ma, M.-J. Li, K. Xu, and Z. He, "Second-order few-mode Raman amplifier for mode-division multiplexed optical communication systems," Optics Express **25**, 810-820 (2017).

33. G. Le Cocq, L. Bigot, A. Le Rouge, M. Bigot-Astruc, P. Sillard, C. Koebele, M. Salsi, and Y. Quiquempois, "Modeling and characterization of a few-mode EDFA supporting four mode groups for mode division multiplexing," Optics express **20**, 27051-27061 (2012).

34. N. Bai, E. Ip, T. Wang, and G. Li, "Multimode fiber amplifier with tunable modal gain using a reconfigurable multimode pump," Optics express **19**, 16601-16611 (2011).

35. G. Lopez-Galmiche, Z. S. Eznaveh, J. Antonio-Lopez, A. V. Benitez, J. R. Asomoza, J. S. Mondragon, C. Gonnet, P. Sillard, G. Li, and A. Schülzgen, "Few-mode erbium-doped fiber amplifier with photonic lantern for pump spatial mode control," Optics letters **41**, 2588-2591 (2016).

36. Y. Jung, Q. Kang, V. Sleiffer, B. Inan, M. Kuschnerov, V. Veljanovski, B. Corbett, R. Winfield, Z. Li, and P. Teh, "Three mode Er 3+ ring-doped fiber amplifier for mode-division multiplexed transmission," Optics Express **21**, 10383-10392 (2013).

37. Y. Jung, E. Lim, Q. Kang, T. May-Smith, N. Wong, R. Standish, F. Poletti, J. Sahu, S. Alam, and D. Richardson, "Cladding pumped few-mode EDFA for mode division multiplexed transmission," Optics express **22**, 29008-29013 (2014).

38.   Z. Zhang, C. Guo, L. Cui, Q. Mo, N. Zhao, C. Du, X. Li, and G. Li, "21 spatial mode erbium-doped fiber amplifier for mode division multiplexing transmission," Optics Letters **43**, 1550-1553 (2018).

39.   S. Wittek, R. B. Ramirez, J. A. Zacarias, Z. S. Eznaveh, J. Bradford, G. L. Galmiche, D. Zhang, W. Zhu, J. Antonio-Lopez, and L. Shah, "Mode-selective amplification in a large mode area Yb-doped fiber using a photonic lantern," Optics Letters **41**, 2157-2160 (2016).

40.   G. Li, N. Bai, N. Zhao, and C. Xia, "Space-division multiplexing: the next frontier in optical communication," Advances in Optics and Photonics **6**, 413-487 (2014).

41.   J. van Weerdenburg, A. Velàzquez-Benitez, R. van Uden, P. Sillard, D. Molin, A. Amezcua-Correa, E. Antonio-Lopez, M. Kuschnerov, F. Huijskens, and H. de Waardt, "10 Spatial mode transmission using low differential mode delay 6-LP fiber using all-fiber photonic lanterns," Optics express **23**, 24759-24769 (2015).

42.   N. K. Fontaine, R. Ryf, H. Chen, A. V. Benitez, J. A. Lopez, R. A. Correa, B. Guan, B. Ercan, R. P. Scott, and S. B. Yoo, "30× 30 MIMO transmission over 15 spatial modes," in *Optical Fiber Communication Conference*, (Optical Society of America, 2015), Th5C. 1.

43.   S. Chandrasekhar, A. Gnauck, X. Liu, P. Winzer, Y. Pan, E. Burrows, B. Zhu, T. Taunay, M. Fishteyn, and M. Yan, "WDM/SDM transmission of 10× 128-Gb/s PDM-QPSK over 2688-km 7-core fiber with a per-fiber net aggregate spectral-efficiency distance product of 40,320 kmb/s/Hz," in *2011 37th European Conference and Exhibition on Optical Communication*, (IEEE, 2011), 1-3.

44.   C. Xia, R. Amezcua-Correa, N. Bai, E. Antonio-Lopez, D. M. Arrioja, A. Schulzgen, M. Richardson, J. Liñares, C. Montero, and E. Mateo, "Hole-assisted few-mode multicore fiber for high-density space-division multiplexing," IEEE Photonics Technology Letters **24**, 1914-1917 (2012).

45.   H. Chen, C. Jin, B. Huang, N. K. Fontaine, R. Ryf, K. Shang, N. Grégoire, S. Morency, R.-J. Essiambre, and G. Li, "Integrated cladding-pumped multicore few-mode erbium-doped fibre amplifier for space-division-multiplexed communications," Nature Photonics **10**, 529-533 (2016).

46.   Y. Mimura, Y. Tsuchida, K. Maeda, R. Miyabe, K. Aiso, H. Matsuura, and R. Sugizaki, "Batch multicore amplification with cladding-pumped multicore EDF," in *European Conference and Exhibition on Optical Communication*, (Optical Society of America, 2012), Tu. 4. F. 1.

47.   J. Sakaguchi, W. Klaus, B. J. Puttnam, J. M. D. Mendinueta, Y. Awaji, N. Wada, Y. Tsuchida, K. Maeda, M. Tadakuma, and K. Imamura, "19-core MCF transmission system using EDFA with shared core pumping coupled via free-space optics," Optics Express **22**, 90-95 (2014).

48. S. Jain, T. Mizuno, Y. Jung, Q. Kang, J. R. Hayes, M. N. Petrovich, G. Bai, H. Ono, K. Shibahara, and A. Sano, "32-core inline multicore fiber amplifier for dense space division multiplexed transmissionsystems," in *ECOC 2016-Post Deadline Paper; 42nd European Conference on Optical Communication*, (VDE, 2016), 1-3.

49. N. K. Fontaine, B. Huang, Z. S. Eznaveh, H. Chen, J. Cang, B. Ercan, A. Veláquez-Benitez, S. Chang, R. Ryf, and A. Schulzgen, "Multi-mode optical fiber amplifier supporting over 10 spatial modes," in *Optical Fiber Communication Conference*, (Optical Society of America, 2016), Th5A. 4.

50. N. K. Fontaine, R. Ryf, J. Bland-Hawthorn, and S. G. Leon-Saval, "Geometric requirements for photonic lanterns in space division multiplexing," Optics express **20**, 27123-27132 (2012).

51. J. Montoya, C. Aleshire, C. Hwang, N. K. Fontaine, A. Velázquez-Benítez, D. H. Martz, T. Fan, and D. Ripin, "Photonic lantern adaptive spatial mode control in LMA fiber amplifiers," Optics Express **24**, 3405-3413 (2016).

52. F. Yaman, N. Bai, B. Zhu, T. Wang, and G. Li, "Long distance transmission in few-mode fibers," Optics Express **18**, 13250-13257 (2010).

53. E. Ip, "Gain equalization for few-mode fiber amplifiers beyond two propagating mode groups," IEEE Photonics Technology Letters **24**, 1933-1936 (2012).

54. T. A. Birks, I. Gris-Sánchez, S. Yerolatsitis, S. Leon-Saval, and R. R. Thomson, "The photonic lantern," Advances in Optics and Photonics **7**, 107-167 (2015).

55. S. G. Leon-Saval, N. K. Fontaine, J. R. Salazar-Gil, B. Ercan, R. Ryf, and J. Bland-Hawthorn, "Mode-selective photonic lanterns for space-division multiplexing," Optics express **22**, 1036-1044 (2014).

56. B. Huang, N. K. Fontaine, R. Ryf, B. Guan, S. G. Leon-Saval, R. Shubochkin, Y. Sun, R. Lingle, and G. Li, "All-fiber mode-group-selective photonic lantern using graded-index multimode fibers," Optics express **23**, 224-234 (2015).

57. A. Velazquez-Benitez, J. Alvarado, G. Lopez-Galmiche, J. Antonio-Lopez, J. Hernández-Cordero, J. Sanchez-Mondragon, P. Sillard, C. Okonkwo, and R. Amezcua-Correa, "Six mode selective fiber optic spatial multiplexer," Optics Letters **40**, 1663-1666 (2015).

58. H. Liu, H. Wen, B. Huang, R. A. Correa, P. Sillard, H. Chen, Z. Li, and G. Li, "Reducing group delay spread using uniform long-period gratings," Scientific reports **8**, 3882 (2018).

59. A. M. Yao and M. J. Padgett, "Orbital angular momentum: origins, behavior and applications," Advances in Optics and Photonics **3**, 161-204 (2011).

60. S. Fürhapter, A. Jesacher, S. Bernet, and M. Ritsch-Marte, "Spiral phase contrast imaging in microscopy," Optics Express **13**, 689-694 (2005).

61. R. Chen, K. Agarwal, C. J. Sheppard, and X. Chen, "Imaging using cylindrical vector beams in a high-numerical-aperture microscopy system," Optics letters **38**, 3111-3114 (2013).

62. X. Hao, C. Kuang, T. Wang, and X. Liu, "Effects of polarization on the de-excitation dark focal spot in STED microscopy," Journal of Optics **12**, 115707 (2010).

63. K. Toyoda, F. Takahashi, S. Takizawa, Y. Tokizane, K. Miyamoto, R. Morita, and T. Omatsu, "Transfer of light helicity to nanostructures," Physical review letters **110**, 143603 (2013).

64. M. P. Lavery, F. C. Speirits, S. M. Barnett, and M. J. Padgett, "Detection of a spinning object using light's orbital angular momentum," Science **341**, 537-540 (2013).

65. Q. Kang, P. Gregg, Y. Jung, E. L. Lim, S.-u. Alam, S. Ramachandran, and D. J. Richardson, "Amplification of 12 OAM modes in an air-core erbium doped fiber," Optics Express **23**, 28341-28348 (2015).

66. Y. Jung, Q. Kang, R. Sidharthan, D. Ho, S. Yoo, P. Gregg, S. Ramachandran, S.-U. Alam, and D. J. Richardson, "Optical orbital angular momentum amplifier based on an air-hole erbium-doped fiber," Journal of Lightwave Technology **35**, 430-436 (2017).

67. Z. S. Eznaveh, J. C. A. Zacarias, J. E. A. Lopez, K. Shi, G. Milione, Y. Jung, B. C. Thomsen, D. J. Richardson, N. Fontaine, and S. G. Leon-Saval, "Photonic lantern broadband orbital angular momentum mode multiplexer," Optics express **26**, 30042-30051 (2018).

68. J. van Weerdenburg, R. Ryf, J. C. Alvarado-Zacarias, R. A. Alvarez-Aguirre, N. K. Fontaine, H. Chen, R. Amezcua-Correa, T. Koonen, and C. Okonkwo, "138 Tbit/s transmission over 650 km graded-index 6-mode fiber," in *2017 European Conference on Optical Communication (ECOC)*, (IEEE, 2017), 1-3.

69. S. G. Leon-Saval, N. K. Fontaine, and R. Amezcua-Correa, "Photonic lantern as mode multiplexer for multimode optical communications," Optical Fiber Technology **35**, 46-55 (2017).

70. S. Yerolatsitis, I. Gris-Sánchez, and T. Birks, "Adiabatically-tapered fiber mode multiplexers," Optics express **22**, 608-617 (2014).

71. A. M. Velázquez-Benítez, J. E. Antonio-López, J. C. Alvarado-Zacarías, N. K. Fontaine, R. Ryf, H. Chen, J. Hernández-Cordero, P. Sillard, C. Okonkwo, and S. G. Leon-Saval, "Scaling photonic lanterns for space-division multiplexing," Scientific reports **8**, 1-9 (2018).

72.   A. Kobyakov, M. Sauer, and D. Chowdhury, "Stimulated Brillouin scattering in optical fibers," Advances in optics and photonics **2**, 1-59 (2010).

73.   D. R. Ponikvar and S. Ezekiel, "Stabilized single-frequency stimulated Brillouin fiber ring laser," Optics letters **6**, 398-400 (1981).

74.   L. Stokes, M. Chodorow, and H. Shaw, "All-fiber stimulated Brillouin ring laser with submilliwatt pump threshold," Optics Letters **7**, 509-511 (1982).

75.   G. Wang, L. Zhan, J. Liu, T. Zhang, J. Li, L. Zhang, J. Peng, and L. Yi, "Watt-level ultrahigh-optical signal-to-noise ratio single-longitudinal-mode tunable Brillouin fiber laser," Optics letters **38**, 19-21 (2013).

76.   J. Wang, Y. Hou, Q. Zhang, D. Jin, R. Sun, H. Shi, J. Liu, and P. Wang, "High-power, high signal-to-noise ratio single-frequency 1 μm Brillouin all-fiber laser," Optics express **23**, 28978-28984 (2015).

77.   S. Smith, F. Zarinetchi, and S. Ezekiel, "Narrow-linewidth stimulated Brillouin fiber laser and applications," Optics letters **16**, 393-395 (1991).

78.   J. Geng, S. Staines, Z. Wang, J. Zong, M. Blake, and S. Jiang, "Highly stable low-noise Brillouin fiber laser with ultranarrow spectral linewidth," IEEE photonics technology letters **18**, 1813-1815 (2006).

79.   Z. Ou, X. Bao, and L. Chen, "Ultranarrow Linewidth Brillouin Fiber Laser," IEEE photonics technology letters **26**(2014).

80.   J. Geng, S. Staines, and S. Jiang, "Dual-frequency Brillouin fiber laser for optical generation of tunable low-noise radio frequency/microwave frequency," Optics letters **33**, 16-18 (2008).

81.   J. Liu, L. Zhan, P. Xiao, G. Wang, L. Zhang, X. Liu, J. Peng, and Q. Shen, "Generation of step-tunable microwave signal using a multiwavelength Brillouin fiber laser," IEEE Photonics Technology Letters **25**, 220-223 (2013).

82.   L. Zhan, J. Ji, J. Xia, S. Luo, and Y. Xia, "160-line multiwavelength generation of linear-cavity self-seeded Brillouin-erbium fiber laser," Optics express **14**, 10233-10238 (2006).

83.   M. H. Al-Mansoori and M. A. Mahdi, "Tunable range enhancement of Brillouin-erbium fiber laser utilizing Brillouin pump preamplification technique," Optics express **16**, 7649-7654 (2008).

84.   X. Heng, J. Gan, Z. Zhang, J. Li, M. Li, H. Zhao, Q. Qian, S. Xu, and Z. Yang, "Transverse mode switchable all-fiber Brillouin laser," Optics letters **43**, 4172-4175 (2018).

85. R. Waldron, "Some problems in the theory of guided microsonic waves," IEEE Transactions on Microwave Theory and Techniques **17**, 893-904 (1969).

86. L. Dong, "Formulation of a complex mode solver for arbitrary circular acoustic waveguides," Journal of lightwave technology **28**, 3162-3175 (2010).

87. W. Schmid, C. Jung, B. Weigi, G. Reiner, R. Michalzik, and K. J. Ebeling, "Delayed self-heterodyne linewidth measurement of VCSELs," IEEE Photonics Technology Letters **8**, 1288-1290 (1996).

88. D. J. Wineland, R. E. Drullinger, and F. L. Walls, "Radiation-pressure cooling of bound resonant absorbers," Physical Review Letters **40**, 1639 (1978).

89. W. Neuhauser, M. Hohenstatt, P. Toschek, and H. Dehmelt, "Optical-sideband cooling of visible atom cloud confined in parabolic well," Physical Review Letters **41**, 233 (1978).

90. D. Kleckner and D. Bouwmeester, "Sub-kelvin optical cooling of a micromechanical resonator," Nature **444**, 75-78 (2006).

91. D. Hempston, J. Vovrosh, M. Toroš, G. Winstone, M. Rashid, and H. Ulbricht, "Force sensing with an optically levitated charged nanoparticle," Applied Physics Letters **111**, 133111 (2017).

92. A. A. Geraci, S. B. Papp, and J. Kitching, "Short-range force detection using optically cooled levitated microspheres," Physical review letters **105**, 101101 (2010).

93. C. M. Caves, "Quantum-mechanical noise in an interferometer," Physical Review D **23**, 1693 (1981).

94. B. S. Sheard, M. B. Gray, C. M. Mow-Lowry, D. E. McClelland, and S. E. Whitcomb, "Observation and characterization of an optical spring," Physical Review A **69**, 051801 (2004).

95. S. Wallentowitz, W. Vogel, I. Siemers, and P. Toschek, "Vibrational amplification by stimulated emission of radiation," Physical Review A **54**, 943 (1996).

96. R. Beardsley, A. Akimov, M. Henini, and A. Kent, "Coherent terahertz sound amplification and spectral line narrowing in a stark ladder superlattice," Physical review letters **104**, 085501 (2010).

97. T. J. Kippenberg and K. J. Vahala, "Cavity optomechanics: back-action at the mesoscale," science **321**, 1172-1176 (2008).

98. K. Vahala, M. Herrmann, S. Knünz, V. Batteiger, G. Saathoff, T. Hänsch, and T. Udem, "A phonon laser," Nature Physics **5**, 682-686 (2009).

99. R. M. Pettit, W. Ge, P. Kumar, D. R. Luntz-Martin, J. T. Schultz, L. P. Neukirch, M. Bhattacharya, and A. N. Vamivakas, "An optical tweezer phonon laser," Nature Photonics **13**, 402-405 (2019).

100. I. S. Grudinin, H. Lee, O. Painter, and K. J. Vahala, "Phonon laser action in a tunable two-level system," Physical review letters **104**, 083901 (2010).

101. G. Bahl, J. Zehnpfennig, M. Tomes, and T. Carmon, "Stimulated optomechanical excitation of surface acoustic waves in a microdevice," Nature communications **2**, 1-6 (2011).

102. W. Renninger, P. Kharel, R. Behunin, and P. Rakich, "Bulk crystalline optomechanics," Nature Physics **14**, 601-607 (2018).

103. R. N. Thurston, "Elastic waves in rods and clad rods," The Journal of the Acoustical Society of America **64**, 1-37 (1978).

104. C. Krischer, "Optical measurements of ultrasonic attenuation and reflection losses in fused silica," The Journal of the Acoustical Society of America **48**, 1086-1092 (1970).

105. P. S. J. Russell, D. Culverhouse, and F. Farahi, "Theory of forward stimulated Brillouin scattering in dual-mode single-core fibers," IEEE journal of quantum electronics **27**, 836-842 (1991).

106. R. G. Smith, "Optical power handling capacity of low loss optical fibers as determined by stimulated Raman and Brillouin scattering," Applied optics **11**, 2489-2494 (1972).